nature structural & molecular biology

ARTICLES

https://doi.org/10.1038/s41594-022-00796-6

Check for updates

Inactive and active state structures template selective tools for the human 5-HT$_{5A}$ receptor

Shicheng Zhang[1], He Chen[2], Chengwei Zhang[2], Ying Yang[3], Petr Popov[4], Jing Liu[2], Brian E. Krumm[1], Can Cao[1], Kuglae Kim[1], Yan Xiong[2], Vsevolod Katritch[5], Brian K. Shoichet[3], Jian Jin[2], Jonathan F. Fay[6] ✉ and Bryan L. Roth[1] ✉

Serotonin receptors are important targets for established therapeutics and drug development as they are expressed throughout the human body and play key roles in cell signaling. There are 12 serotonergic G protein-coupled receptor members encoded in the human genome, of which the 5-hydroxytryptamine (5-HT)$_{5A}$ receptor (5-HT$_{5A}$R) is the least understood and lacks selective tool compounds. Here, we report four high-resolution (2.73–2.80 Å) structures of human 5-HT$_{5A}$Rs, including an inactive state structure bound to an antagonist AS2674723 by crystallization and active state structures bound to a partial agonist lisuride and two full agonists, 5-carboxamidotryptamine (5-CT) and methylergometrine, by cryo-EM. Leveraging the new structures, we developed a highly selective and potent antagonist for 5-HT$_{5A}$R. Collectively, these findings both enhance our understanding of this enigmatic receptor and provide a roadmap for structure-based drug discovery for 5-HT$_{5A}$R.

Serotonin (5-HT) is a neurotransmitter essential for the regulation of mood, perception, feeding, anxiety and gastrointestinal and cardiac functions as well as the actions of many drugs useful in treating neuropsychiatric and other disorders[1,2]. To mediate these actions, a large family of 5-HT receptors has evolved including 12 G protein-coupled receptors (GPCRs) divided into six major families (namely, 5-HT$_1$, 5-HT$_2$, 5-HT$_4$, 5-HT$_5$, 5-HT$_6$ and 5-HT$_7$)[1,2]. Of these, the human 5-HT$_{5A}$R is the most enigmatic and least understood. Based on gene knockout and expression analysis as well as studies with relatively nonselective antagonists, 5-HT$_{5A}$R has been implicated in the actions of the psychedelic drug lysergic acid diethylamide (LSD)[3], the modulation of pain[4], antidepressant drug actions[5] and anxiety[1]. These effects are consistent with the wide distribution of 5-HT$_{5A}$Rs in the human brain, with the highest expression in the cortex and limbic areas[6]. Although there are potential tool compounds available to interrogate 5-HT$_{5A}$ function, the most widely used compounds, SB-699551, ASP5736 and AS2674723, are nonselective and interact with various 5-HT and related biogenic amine receptors[7–9], making the pharmacological exploration of the role of 5-HT$_{5A}$R problematic. More recently, an arrestin-biased partial agonist of 5-HT$_{5A}$R, UCSF678, was developed based on the homolog model of 5-HT$_{5A}$R, which displayed a more restricted, albeit still considerable, off-target profile[10].

The 5-HT$_{5A}$R also has an unusual pharmacological profile with the highest affinity for ergots and ergolines and the synthetic agonist 5-CT[11,12] and low affinity for most other agonists and antagonists of 5-HT receptors. In addition, the signaling pathways downstream of 5-HT$_{5A}$R are not fully elucidated, although coupling to a pertussis toxin-sensitive G protein has been demonstrated[13]. Finally, the structural basis for the unique pharmacology of 5-HT$_{5A}$R is unknown, as, given its relatively low sequence identity with other 5-HT receptors, it is likely that the ligand-recognition site is distinct (Extended Data Fig. 1a). Given this lack of fundamental knowledge regarding the structure, function and pharmacology of 5-HT$_{5A}$R as well as its clear importance for brain function, we determined the structures of the inactive state and the active G protein-coupled state by X-ray crystallography and single-particle cryo-EM, respectively. We further used the inactive state structure to template the discovery of a potent and selective 5-HT$_{5A}$R antagonist. In sum, these studies will accelerate the search for selective 5-HT$_{5A}$R agonists and antagonists as potential therapeutics for a number of neuropsychiatric disorders.

Results

Structures of antagonist- and agonist-bound 5-HT$_{5A}$R complexes. We initially obtained an inactive state structure of 5-HT$_{5A}$R in complex with the antagonist AS2674723. To achieve this, three modifications of 5-HT$_{5A}$ were applied: (1) the N-terminal 22 residues were truncated; (2) protein PGS (the catalytic domain of *Pyrococcus abyssi* glycogen synthase)[14] was fused to the third intracellular loop; and (3) two thermostabilizing mutations (corresponding to D86$^{2\times50}$N and I299$^{6\times49}$A; superscript is the generic residue number in the GPCR database[15]) were also introduced into the construct based on both extensive computational predictions and experimental validation[16] (Supplementary Fig. 1). Eventually, the structure of the 5-HT$_{5A}$R–AS2674723 complex was solved using molecular replacement and refined to a resolution of 2.8 Å (Table 1). There is one 5-HT$_{5A}$R–AS2674723 complex in the asymmetric unit, in which the ligand and most residues of the receptor, except intracellular loop 1 and helix 8 (H8), are well defined (Fig. 1a).

To gain insight into the activation mechanism of 5-HT$_{5A}$R, we also attempted to determine the active state structure of 5-HT$_{5A}$R.

[1]Department of Pharmacology, School of Medicine, University of North Carolina at Chapel Hill, Chapel Hill, NC, USA. [2]Mount Sinai Center for Therapeutics Discovery, Departments of Pharmacological Sciences, Oncological Sciences and Neuroscience, Tisch Cancer Institute, Icahn School of Medicine at Mount Sinai, New York, NY, USA. [3]Department of Pharmaceutical Sciences, University of California San Francisco, School of Medicine, San Francisco, CA, USA. [4]iMolecule, Skolkovo Institute of Science and Technology, Moscow, Russia. [5]Departments of Quantitative and Computational Biology and Chemistry, Bridge Institute, USC Michelson Center for Convergent Biosciences, University of Southern California, Los Angeles, CA, USA. [6]Department of Biochemistry and Biophysics, University of North Carolina at Chapel Hill School of Medicine, Chapel Hill, NC, USA. ✉e-mail: fayj@unc.edu; bryan_roth@med.unc.edu

Table 1 | Data collection and refinement statistics

	5-HT$_{5A}$R–AS2674723[a] (PDB 7UM4)
Data collection	
Space group	$P2_12_12$
Cell dimensions	
a, *b*, *c* (Å)	135.3, 42.5, 94.8
α, β, γ (°)	90, 90, 90
Resolution (Å)	50.0–2.8 (2.90–2.80)[b]
R_{merge} (%)	30.7 (102.9)
I/σ (I)	5.8 (1.1)
$CC_{1/2}$ (%)	95.4 (55.4)
Completeness (%)	99.2 (97.2)
Redundancy	6.6 (3.6)
Refinement	
Resolution (Å)	50.0–2.8 (2.91–2.81)
No. reflections	13,696 (1,108)
R_{work} / R_{free} (%)	22.9 / 27.1
No. atoms	3,633
Protein	3,539
Lipids	60
Water	8
B factors (Å^2)	67.6
Protein	67.6
AS2674723	62.5
Lipids	71.4
Water	56.5
R.m.s. deviations	
Bond lengths (Å)	0.006
Bond angles (°)	0.78

[a]The number of crystals is 17. [b]Values in parentheses are for the highest-resolution shell.

First, by using the TRUPATH biosensor platform[17], we found that 5-HT$_{5A}$R effectively couples to every member of the $G_{i/o}$ family (G_{i1-i3} and G_{oA-oB}) with the exception of G_z and G_{ust}. We also found that 5-HT$_{5A}$R can activate G_{15}, a subunit in the G_q family when these are coexpressed in HEK293T cells (Extended Data Fig. 1b). As the activation potencies between the G_{i1-i3} and G_{oA-oB} subfamilies for 5-HT$_{5A}$R are comparable and miniG_o has been used in the structural determination of active state 5-HT$_{1B}$R[18] successfully, thus, miniG_o was also applied for active state structural studies of 5-HT$_{5A}$R. Additionally, the mutation corresponding to H146$^{34\times50}$P was introduced into the 5-HT$_{5A}$R construct to improve the stability of the complex. The 5-HT$_{5A}$R–miniG_o complexes were assembled by coexpression of 5-HT$_{5A}$R with miniG_o and Gβ_1 and Gγ_2 subunits via the NanoBiT tethering system[19]. Eventually, the structures of 5-HT$_{5A}$R–miniG_o bound to 5-CT, lisuride and methylergometrine were determined at resolutions of 2.73 Å, 2,79 Å and 2.75 Å, respectively (Table 2 and Extended Data Fig. 2). The overall structures of these three agonist-bound 5-HT$_{5A}$R complexes are similar to each other with root-mean-square deviation (RMSD) values lower than 0.3 Å for the whole-complex comparisons between each structure (Fig. 1b and Extended Data Fig. 3a–c).

AS2674723 recognition by 5-HT$_{5A}$R. Overall, the recognition of AS2674723 by 5-HT$_{5A}$R is primarily based on its three chemical moieties: a tetrahydroisoquinoline ring, a positively charged guanidine group and a trifluorophenyl ring, which occupies the orthosteric binding pocket, extended binding pocket 1 and extended binding pocket 2 (EBP2), respectively (Fig. 2a and Extended Data Fig. 4a). The tetrahydroisoquinoline ring mainly interacts with F301$^{6\times51}$ and F302$^{6\times52}$ by $\pi-\pi$ interactions and with V122$^{3\times33}$ and C125$^{3\times36}$ through hydrophobic contacts (Fig. 2a). Also, the guanidine group forms a salt bridge with E101$^{2\times64}$, which is accompanied by a rotation and shift of the extracellular end of transmembrane helix (TM)2 in comparison with the active state 5-HT$_{5A}$R structures (Figs. 2a and 5d). In addition, E101$^{2\times64}$, D121$^{3\times32}$, Q193^{ECL2} and Y328$^{7\times42}$ also have hydrophilic interactions with this guanidine group. Additionally, hydrophobic interactions between the side chain of L324$^{7\times38}$ and the guanidine group were also observed (Fig. 2a). Lastly, the trifluorophenyl ring forms extensive contacts with surrounding residues of EBP2, including V194^{ECL2}, R196^{ECL2}, Y200$^{5\times39}$, S204$^{5\times43}$, T205$^{5\times44}$ and E305$^{6\times55}$ (Fig. 2a and Extended Data Fig. 4a).

To gain insight into the selectivity of AS2674723, we determined its binding affinities with aminergic receptors and carried out mutagenesis studies on the residues interacting with AS2674723. These screening results showed that 5-HT$_{5A}$R (0.6 nM) and 5-HT$_7$R (1.3 nM) were the primary targets of AS2674723. Additionally, 5-HT$_{1A}$R (33 nM), 5-HT$_{1B}$R (15 nM), 5-HT$_{1D}$R (50 nM), α_{2A}AR (25 nM) and α_{2C}AR (52 nM) also showed high affinities for AS2674723 (Extended Data Fig. 5a). In an alanine mutagenesis study, (1) D121$^{3\times32}$A, F301$^{6\times51}$A and Y328$^{7\times42}$A mutants lost their binding ability to the radioligand ^{3}H[LSD], and thus no binding affinities were determined for AS2674723; (2) V122$^{3\times33}$A and L324$^{7\times38}$A mutations severely reduced the binding affinities by 99-fold and 66-fold, respectively; (3) E101$^{2\times64}$A, C125$^{3\times36}$A, Y200$^{5\times39}$A, T205$^{5\times44}$A and A208$^{5\times461}$G moderately affected the binding affinities by more than fivefold; and (4) the other mutations (Q193^{ECL2}A, V194^{ECL2}A, R196^{ECL2}A, S204$^{5\times43}$A, F302$^{6\times52}$A and E305$^{6\times55}$A) had modest effects on binding affinities (Extended Data Fig. 5b–c).

Interestingly, by combining the above mutagenesis data with sequence analysis, we found that L324$^{7\times38}$ was a less conserved residue in the serotonin receptor family with the exception of 5-HT$_4$R and 5-HT$_7$R, and the L324$^{7\times38}$A mutation dramatically affected the binding affinity of AS2674723, which might suggest a crucial role for its selectivity (Extended Data Figs. 5b and 6a). The mutants with L324$^{7\times38}$N (5-HT$_{1A}$R) and L324$^{7\times38}$T (5-HT$_{1B}$R, 5-HT$_{1D}$R and 5-HT$_{1E}$R) substitutions displayed similar effects as L324$^{7\times38}$A, both of which had reduced binding affinities for AS2674723 by more than 50-fold (Extended Data Figs. 5b and 6a). Additionally, E101$^{2\times64}$, which forms a specific salt bridge with the guanidine group of AS2674723, is another unconserved residue, suggesting a potential role in the selectivity of this ligand. Three mutations (E101$^{2\times64}$Q, E101$^{2\times64}$T and E101$^{2\times64}$I) mimicking other members of the 5-HT receptor family displayed similar effects as E101$^{2\times64}$A, reducing the binding affinity of AS2674723 from 7.4-fold to 13.2-fold (Extended Data Figs. 5b and 6a). Importantly, 5-HT$_7$R, the primary off-target of AS2674723, has an aspartate instead of a glutamate at position 2×64, which could potentially form similar electrostatic interactions with the guanidine group of AS2674723 (Extended Data Fig. 6a). This was also consistent with our mutagenesis data, as the E101$^{2\times64}$D substitution did not alter AS2674723-binding affinity (Extended Data Fig. 5b). In sum, these data indicated that the interactions between E101$^{2\times64}$ and AS2674723 are unique and potentially useful for selective drug development against 5-HT$_{5A}$R. Lastly, the C125$^{3\times36}$S and S204$^{5\times43}$G mutations, both of which were mutated to the feature residues of the 5-HT$_2$ subfamily, also showed moderate effects on the binding affinities (Extended Data Figs. 5b and 6a). Thus, these differences further strengthened the selectivity of AS2674723 for 5-HT$_{5A}$R over the 5-HT$_2$ receptors. In conclusion, these data together revealed the molecular mechanism of the selectivity of AS2674723 for 5-HT$_{5A}$R and provided the basis for further selective ligand development, which is explained below.

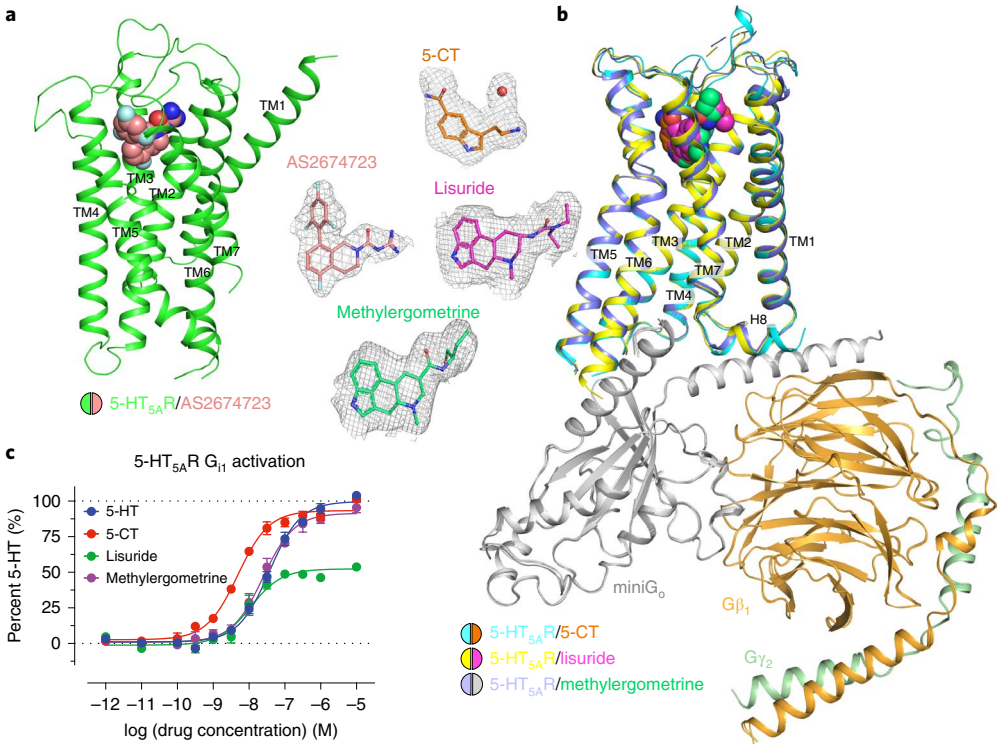

Fig. 1 | Structures of the 5-HT$_{5A}$R complexes. a, Crystal structure of the inactive state 5-HT$_{5A}$R in complex with an antagonist, AS2674723. **b**, Superposition of three cyro-EM structures of 5-HT$_{5A}$R–miniG$_o$ complexes in complex with 5-CT, lisuride and methylergometrine, respectively. The ligands in complexes are shown in spheres within cartoon diagrams of receptors and G proteins. Next to the structural models of 5-HT$_{5A}$R complexes, ligands are shown in stick models surrounded by electron density for the antagonist AS2674723 or EM maps for agonists 5-CT, lisuride and methylergometrine, respectively. Density maps are shown as gray meshes. **c**, Bioluminescence resonance energy transfer (BRET)2 G$_{i1}$-activation assay of 5-HT$_{5A}$R stimulated with the agonists 5-HT, 5-CT, lisuride and methylergometrine. Data were normalized to percent of 5-HT. See Supplementary Table 1 for fitted parameter values that represent mean ± s.e.m. of $n = 4$ biological replicates.

Mode of agonist recognition at the 5-HT$_{5A}$R. In the 5-CT-bound 5-HT$_{5A}$R structure, a featured water molecule interacting with the amino group of 5-CT and D121$^{3\times32}$ was revealed by clear density (Fig. 1b). However, the position was not matched to the water molecules in a prior apo-5-HT$_{1A}$R structure, with the closest one being around 1.6 Å away (Extended Data Fig. 4c). Overall, 5-CT adopts a binding pose in the orthosteric pocket similar to that of 5-HT in the structure of the 5-HT$_{1A}$R–5-HT complex[20]. Notably, the amide group of 5-CT extends to the EBP2 and forms hydrogen bonds with S204$^{5\times43}$ and E305$^{6\times55}$. In a previous report, E$^{6\times55}$ was thought to block the binding of 5-CT to the pocket of 5-HT$_{1E}$R or 5-HT$_{1F}$R via its relatively larger side chain[20]. In our 5-HT$_{5A}$R–5-CT structure, we found that the density map for the carboxyl group of E305$^{6\times55}$ was not evident, suggesting that the interaction between the amide group with E305$^{6\times55}$ was unstable (Extended Data Fig. 4d). Our mutagenesis data also showed that the E305$^{6\times55}$A mutation failed to show a large effect on the activation of G$_{i1}$ signaling (Fig. 2e). Together, these data indicate that E305$^{6\times55}$ does not play an important role in 5-HT$_{5A}$R activation by 5-CT.

Compared to E305$^{6\times55}$, residue S204$^{5\times43}$ might play a key role in the 5-CT selectivity, as it has a specific hydrogen bond with the amide group of 5-CT in our 5-HT$_{5A}$R–5-CT structure but no observed interactions with 5-HT in the 5-HT$_{1A}$R–5-HT structure[20]. Moreover, sequence alignment showed that it was a serine conserved in 5-HT$_1$Rs, 5-HT$_{5A}$R and 5-HT$_7$R at position 5×43, whereas it was a glycine in the 5-HT$_2$Rs, a cysteine in 5-HT$_4$R and an alanine in 5-HT$_6$R. As none of these three residues (Gly, Cys and Ala) could form a hydrogen bond with the amide group of 5-CT, this may lead to lower binding affinities of 5-CT with the 5-HT$_2$, 5-HT$_4$ and 5-HT$_6$ subfamilies (Extended Data Figs. 4i and 6a). To validate the role of S204$^{5\times43}$ in the 5-CT selectivity, three related mutants (with S204$^{5\times43}$A, S204$^{5\times43}$G and S204$^{5\times43}$C) were generated and tested in the G$_{i1}$-activation assay with 5-HT and 5-CT simultaneously. The results showed that the S204$^{5\times43}$A and S204$^{5\times43}$G mutations showed modest effects on both the potency and efficacy of the G$_{i1}$ activation by 5-HT but dramatically reduced the potency of G$_{i1}$ activation by 5-CT (Fig. 2f). Furthermore, the mutation S204$^{5\times43}$C severely affected G$_{i1}$ activation by both 5-HT and 5-CT, which was also consistent with the relatively low affinity of 5-HT with 5-HT$_4$R[21] (Fig. 2f and Extended Data Fig. 4i). Our structural and functional data together suggest a crucial role of S204$^{5\times43}$ in the selectivity of 5-CT in the 5-HT family.

Lisuride has been reported to have a high affinity for 5-HT$_{5A}$R[22], and we found that it is a partial agonist for G$_i$ signaling activation (Fig. 1c). Overall, lisuride adopts a pose largely similar to that of the full agonist methylergometrine, another ergoline scaffold compound, both of which occupy the orthosteric pocket by the ergoline ring and extended binding pocket 1 by their substitutions (Fig. 2c,d and Extended Data Fig. 4a). The key feature of the binding mode of lisuride is the extensive and strong interactions with D121$^{3\times32}$, which leads to several unique properties of lisuride for G$_{i1}$ activation (Fig. 2c,e). For example, residue F301$^{6\times51}$ is a strictly conserved residue across the serotonin family and is essential for ligand binding and receptor activation[23] (Extended Data Fig. 6a). Our mutagenesis data showed that the mutation F301$^{6\times51}$A did abolish the G$_{i1}$-activation abilities of 5-HT, 5-CT and methylergometrine but only slightly affected G$_{i1}$ activation by lisuride, which indicated that the activation by lisuride was not highly

Table 2 | Cryo-EM data collection, refinement and validation statistics

Structures	5-HT$_{5A}$R–miniG$_o$, 5-CT (EMD-26597, PDB 7UM5)	5-HT$_{5A}$R–miniG$_o$, lisuride (EMD-26598, PDB 7UM6)	5-HT$_{5A}$R–miniG$_o$, methylergometrine (EMD-26599, PDB 7UM7)
Data collection and processing			
Magnification	45,000	45,000	45,000
Voltage (kV)	200	200	200
Electron exposure (e$^-$/Å^2)	29.07	43.8	47.4
Defocus (mean ± s.d.) (μm)[a]	1.2 (0.3)	1.1 (0.3)	1.2 (0.4)
Defocus range (μm)[a]	0.3–2.3	0.1–2.2	0.1–2.9
Pixel size (Å)	0.91	0.91	0.91
Symmetry imposed	C1	C1	C1
Initial particle images (no.)	947,828	562,323	1,580,364
Final particle images (no.)	304,291	226,599	634,138
Map resolution (Å)	2.73	2.79	2.75
FSC threshold 0.143	0.143	0.143	0.143
FSC threshold	0.143	0.143	0.143
Map resolution range (Å)	2.4–5.6	2.4–5.3	2.4–5.1
Refinement			
Initial model used (PDB code)	6G79	7UM5	7UM5
Model resolution (Å)[b]	2.94	2.93	2.96
FSC threshold	0.5	0.5	0.5
FSC threshold	0.5	0.5	0.5
Model resolution range (Å)	2.4–5.6	2.4–5.3	2.4–5.1
Map sharpening *B* factor (Å^2)	85.5	82.5	91.6
Model composition			
Non-hydrogen atoms	8,276	8,178	8,167
Protein residues	1,105	1,094	1,089
Ligands	1	1	1
B factors (Å^2)			
Protein	48.83	52.27	49.56
Ligand	40.77	52.22	46.42
Water	43.77	-	-
R.m.s. deviations			
Bond lengths (Å)	0.002	0.003	0.003
Bond angles (°)	0.475	0.515	0.516
Validation			
MolProbity score	1.12	1.14	1.29
Clashscore	2.10	1.82	2.44
Poor rotamers (%)	0.00	0.00	0.00
Ramachandran plot			
Favored (%)	97.24	96.74	96.16
Allowed (%)	2.76	3.26	3.84
Disallowed (%)	0.00	0.00	0.00

[a]Underfocus positive. [b]Resolution estimates from cryoSPARC auto-corrected gold-standard Fourier shell correlation.

dependent on the π–π interaction between F301$^{6\times51}$ and the ergoline ring (Fig. 2e). In other words, these weaker interactions between lisuride and TM6 might also result in the weaker 5-HT$_{5A}$R-activation ability of lisuride. Another difference is that, compared with 5-CT and methylergometrine, the indole ring of lisuride is shifted upward, leading to a weaker hydrogen bond with T126$^{3\times37}$, a crucial residue in activating 5-HT$_{5A}$R (Fig. 2c–e and Extended Data Fig. 4a,e–g). In sum, compared with the full agonists, the weaker interactions between lisuride and TM3 and TM6 might lead to its partial agonism.

Inactive–active state 5-HT$_{5A}$R transitions. Structural alignment of the inactive 5-HT$_{5A}$R structure with 5-HT$_{1B}$R–ergotamine (RMSD, 1.01 Å for 172 Cα) and 5-HT$_{2A}$R–methiothepin (RMSD, 1.72 Å for

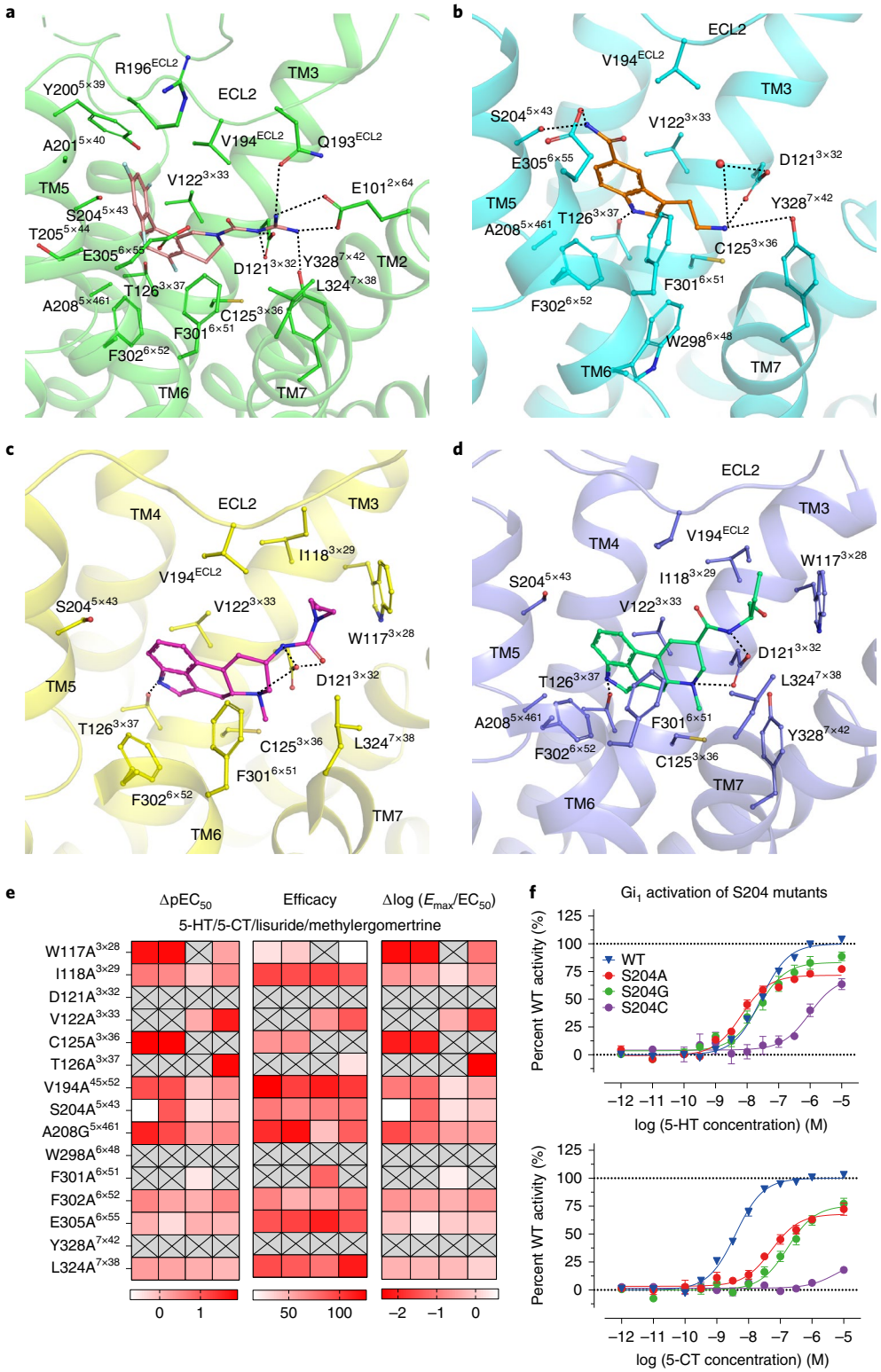

Fig. 2 | Ligand-specific interactions with 5-HT$_{5A}$R. a–d, Specific residues in the binding pockets that interact with AS2674723 (**a**), 5-CT (**b**), lisuride (**c**) and methylergometrine (**d**), respectively. The salt bridge and hydrogen bond interactions are shown as black dashed lines. **e**, Heatmap of data from mutagenesis studies showing the effects of orthosteric site residues in the G_{i1}-activation assay. Boxes marked with 'X' indicate 'not detected', as no appreciable signal was detected. See Supplementary Table 2 for fitted parameter values that represent mean ± s.e.m. of $n = 3$ biological replicates. Surface expression levels of the WT and related mutant 5-HT$_{5A}$Rs were determined by ELISA assay. The mutants with W117A, W298A and Y328A substitutions display significantly low surface expression levels (less than 50% of WT). See Extended Data Fig. 10 for details. EC_{50}, half-maximum effective concentration. **f**, Mutagenesis study of residue S204 of 5-HT$_{5A}$R stimulated with either 5-HT or 5-CT. Data have been normalized to percent of WT 5-HT$_{5A}$R values. See Supplementary Table 3 for fitted parameter values that represent mean ± s.e.m. of at least three biological replicates.

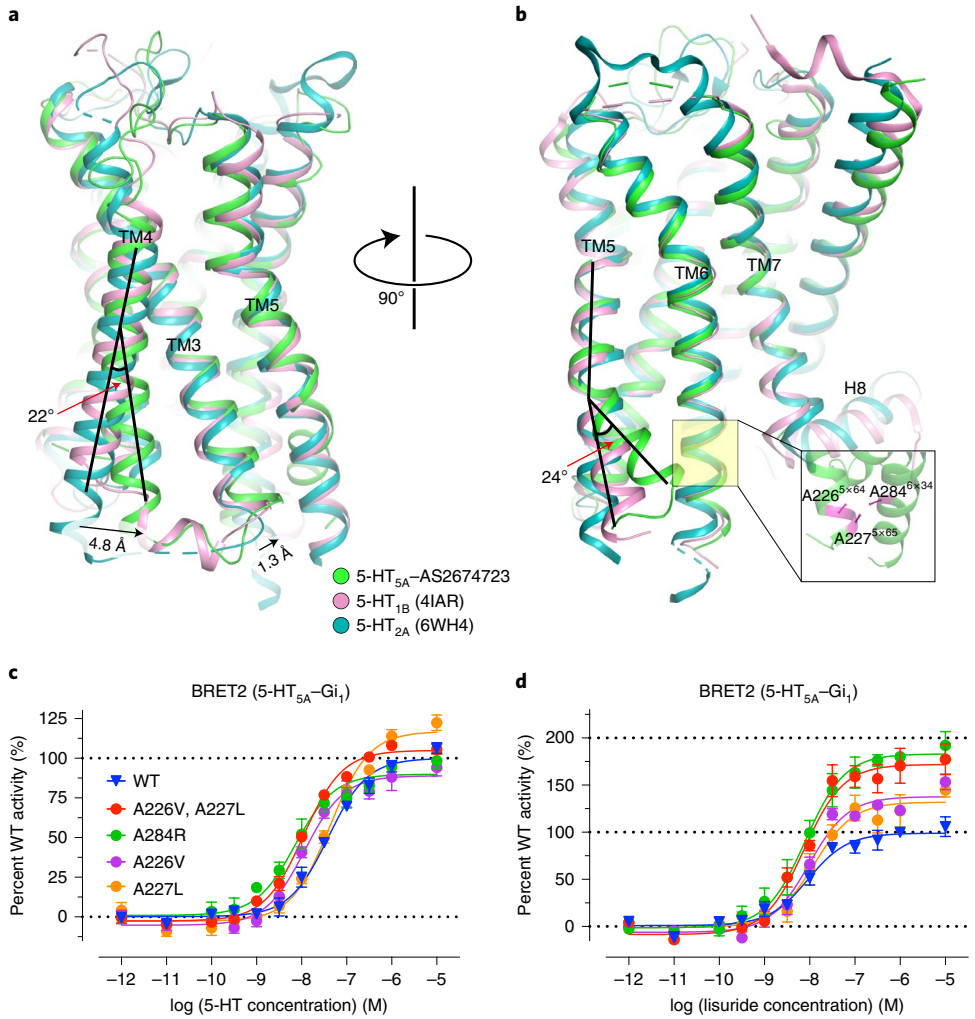

Fig. 3 | Structural comparison between inactive state 5-HT$_{5A}$R and 5-HT$_{1B}$R and 5-HT$_{2A}$R. a,**b**, Superpositions of the 5-HT$_{5A}$R-AS2674723 structure with 5-HT$_{1B}$R-ergotamine (4IAR) and 5-HT$_{2A}$R-methiothepin (6WH4) structures. The bending of TM4 (**a**) and the kinked structure of TM5 (**b**) in inactive state 5-HT$_{5A}$R at the intracellular side. The inset shows the 3A cluster (A226, A227 and A284; shown in stick model and colored in magenta) on the interface between TM5 and TM6. **c**,**d**, BRET2 G_{i1}-activation assay of WT and mutant 5-HT$_{5A}$Rs stimulated with 5-HT (**c**) and lisuride (**d**). See Supplementary Table 4 for fitted parameter values that represent mean ± s.e.m. of $n = 3$ biological replicates.

168 Cα) structures revealed substantial structural differences in the TM3, TM4 and TM5 regions (Fig. 3a,b). Specifically, in comparison with 5-HT$_{1B}$R, the TM3 of 5-HT$_{5A}$R shifts to the TM5 side by 1.3 Å (Cα of T144$^{3\times55}$) and the TM4 of 5-HT$_{5A}$R shifts downward by 0.8 Å (Cα of V175$^{4\times51}$) and bends to the TM3 side around 22° (Cα of K/C$^{4\times40}$ to the Cα of L172$^{4\times48}$) at the intracellular side (Fig. 3a). In the TM5 region, notably, the intracellular end of TM5 of 5-HT$_{5A}$R shows a kinked structure (around 24° rotation compared to 5-HT$_{1B}$R, Cα of K/R$^{5\times66}$ to the Cα of W221$^{5\times59}$) and forms close interactions with the intracellular end of TM6 (Fig. 3b). In particular, this hydrophobic interface is composed of three alanines (A226$^{5\times64}$, A227$^{5\times65}$ and A284$^{6\times34}$, namely, the 3A cluster) (Fig. 3b). Meanwhile, sequence alignment analysis showed that this 3A cluster is not conserved in the 5-HT receptor family, with only 5-HT$_{1E}$R, 5-HT$_{1F}$R and 5-HT$_{7}$R having the same pattern (Extended Data Fig. 6b). However, none of these three receptors have published inactive state structures. This kinked TM5 may block the outward displacement of TM6 upon transducer coupling and thus increase the activation energy barrier (Figs. 3b and 5c).

To test this hypothesis, we mutated the alanine to a bigger side chain residue and determined whether G_i-activation signaling was altered. Combined with the sequence and structural analyses, we made three single mutants (with A226$^{5\times64}$V, A227$^{5\times65}$L and A284$^{6\times34}$R) and one double mutant (with A226$^{5\times64}$V and A227$^{5\times65}$L) and analyzed their G_{i1} signaling activities (Extended Data Figs. 3d,e and 6b). The results showed that the A227$^{5\times65}$L mutation increased the efficacy of 5-HT-stimulated G_{i1} activation by 20%, while A226$^{5\times64}$V, A284$^{6\times34}$R and the double mutation greatly improved the potency by more than 30-fold (Fig. 3c). More interestingly, all the mutations improved the efficacy of lisuride by 1.36–1.88-fold, making it a full agonist (Fig. 3d). Furthermore, we tested this double mutant in G_{i1} signaling activation and β-arrestin 2-recruitment assays with multiple ligands. The results showed that the efficacies could be dramatically improved to the full agonist level for the partial agonists in the G_{i1}-activation assay, and all the efficacies were significantly improved by at least three-fold in the β-arrestin 2-recruitment assay (Extended Data Fig. 7). Thus, this double mutation significantly potentiated G protein and β-arrestin signaling pathways and would be useful in drug screening for 5-HT$_{5A}$R in the future. These structural and functional data together might suggest a self-inhibitory role of the TM5 kink in 5-HT$_{5A}$R signaling activation.

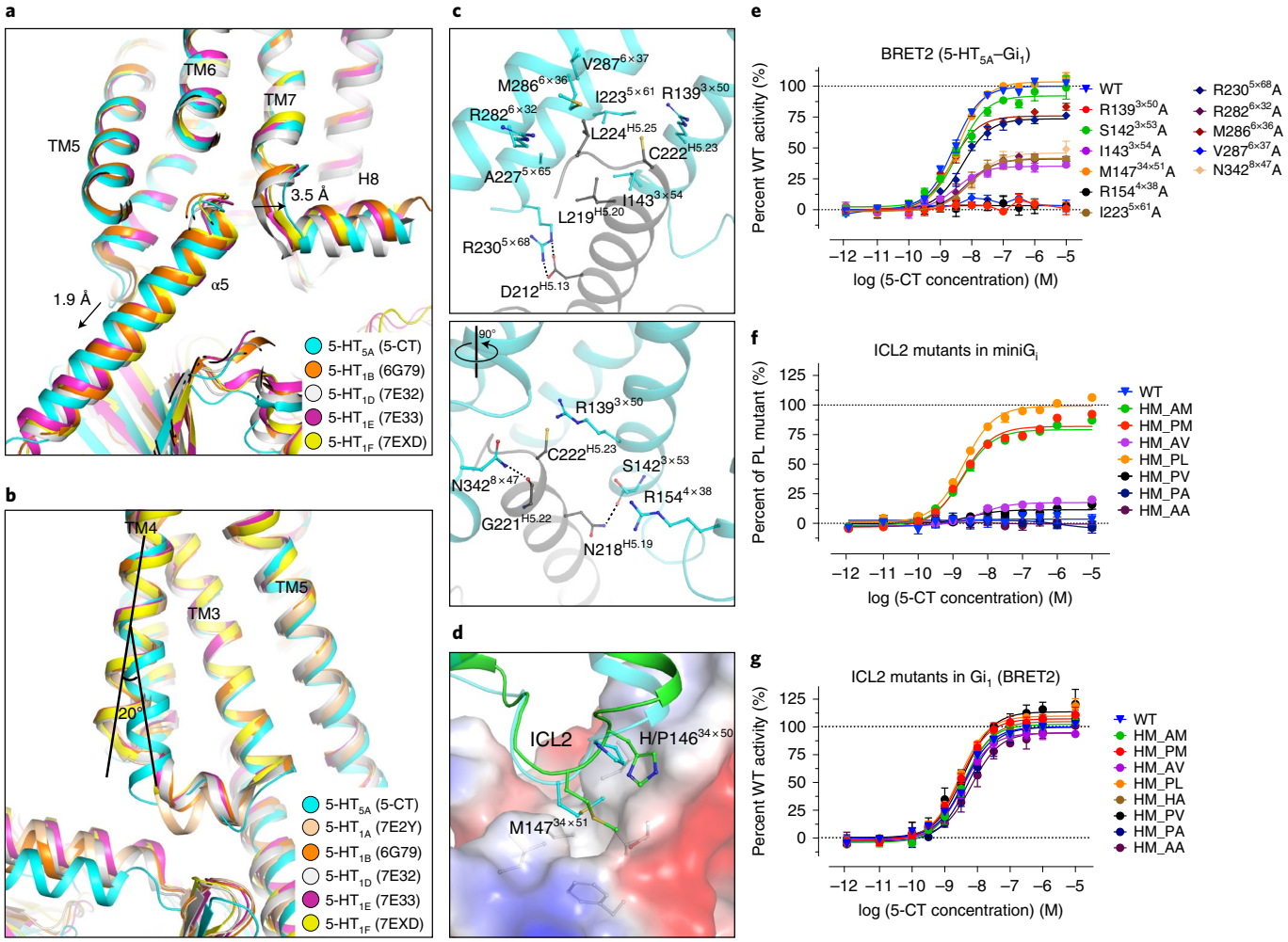

Fig. 4 | The 5-HT$_{5A}$R–miniG$_o$ interface. a,**b**, Superposition of the 5-CT-bound 5-HT$_{5A}$R structure with the active state 5-HT$_1$ structures. **a**, Structural comparison of the G protein-binding mode between 5-HT$_{5A}$R and 5-HT$_1$Rs. **b**, TM4 bending was also observed in the active 5-HT$_{5A}$R structure. **c**, Detailed interactions between 5-HT$_{5A}$R and the α5 helix of miniG$_o$. Salt bridge interactions and hydrogen bonds are depicted as black dashed lines. **d**, The interface between the ICL2 of 5-HT$_{5A}$R and the miniG$_o$ protein. H/P146$^{34\times50}$ represents a histidine or proline in the AS2674723-bound 5-HT$_{5A}$R structure or the 5-CT-bound 5-HT$_{5A}$R structure, respectively. Inactive and active 5-HT$_{5A}$Rs are shown as ribbon models, and the miniG$_o$ shows the electrostatic surface. **e**, BRET2 validation of the interface residues of 5-HT$_{5A}$R. See Supplementary Table 5 for fitted parameter values that represent the mean ± s.e.m. of at least three biological replicates**. f**,**g**, Mutagenesis analysis of ICL2 residues H146 and M147 of 5-HT$_{5A}$R by the BRET1 recruitment assay (**f**) and the BRET2 dissociation assay (**g**). Definitions of curves to the right of each graph indicate mutations, for example, HM_AM indicates a single mutation of H146A, while HM_AA indicates a double mutation of H146A and M147A. HM_PL indicates the double mutation of H146P and M147L. See Supplementary Table 6 for fitted parameter values that represent the mean ± s.e.m. of at least three biological replicates. The surface expression levels of the WT and related mutant 5-HT$_{5A}$Rs were determined by ELISA assay. Of these mutants, those with R154$^{4\times38}$ and V287$^{6\times37}$ substitutions had significantly lower levels than the WT 5-HT$_{5A}$R (less than 50%). See Extended Data Fig. 10 for details.

The 5-HT$_{5A}$R–miniG$_o$ complex interface. The overall binding mode of G protein in 5-HT$_{5A}$R is similar to other 5-HT1 subfamily active state structures with modest differences observed in the α5 helix of miniG$_o$ and H8 of the receptor. Specifically, the α5 helix of miniG$_o$ in the 5-CT-bound 5-HT$_{5A}$R complex is shifted outward by around 0.9 Å (Cα of H$^{5.11}$, compared to the 5-HT$_{1A}$R–G$_i$ complex) and 1.9 Å (compared to the other 5-HT$_1$R complexes) (Fig. 4a and Extended Data Fig. 3f). Additionally, H8 of 5-HT$_{5A}$R is displaced outward by 3.5 Å (Cα of F341$^{7\times56}$) compared to the 5-HT$_{1B}$R structure (Cα of S372$^{7\times56}$) (Fig. 4a). Of note, a similar bending of TM4 is also observed in the comparison of active state 5-HT$_{5A}$R structures with 5-HT$_1$R structures, as in the comparison of inactive state structures (Fig. 4b). We found that R$^{34\times57}$ in the second intracellular loop (ICL2) forms a salt bridge with D$^{3\times49}$ of the DRY motif in all 5-HT$_1$R–G protein complexes, while it is a threonine instead of an arginine at position 34×57 in 5-HT$_{5A}$R (Extended Data Fig. 3g). However, the adjacent R154$^{4\times38}$ residue was observed to engage in an equivalent salt bridge with D$^{3\times49}$ (Extended Data Fig. 3g–h). Thus, this unique sequence composition of the ICL2 of 5-HT$_{5A}$R causes distinct TM4 bending. Moreover, this salt bridge interaction between R154$^{4\times38}$ and D138$^{3\times49}$ was also essential for agonist-activated G$_i$ signaling for 5-HT$_{5A}$R (Fig. 4e).

The major interface between 5-HT$_{5A}$R and miniG$_o$ could be divided into two regions: one is dominantly mediated by the α5 helix of miniG$_o$ and the other by the ICL2 of 5-HT$_{5A}$R (Fig. 4c,d). In the α5 helix region, we observed several hydrophilic interactions, including a salt bridge interaction between R230$^{5\times68}$ and D212$^{H5.13}$ and hydrogen bonds between S142$^{3\times53}$ (main chain) and N342$^{8\times47}$ of the receptor and N218$^{H5.19}$ and G221$^{H5.22}$ of G protein, respectively (Fig. 4c). Additionally, L219$^{H5.20}$ and L224$^{H5.25}$ of miniG$_o$

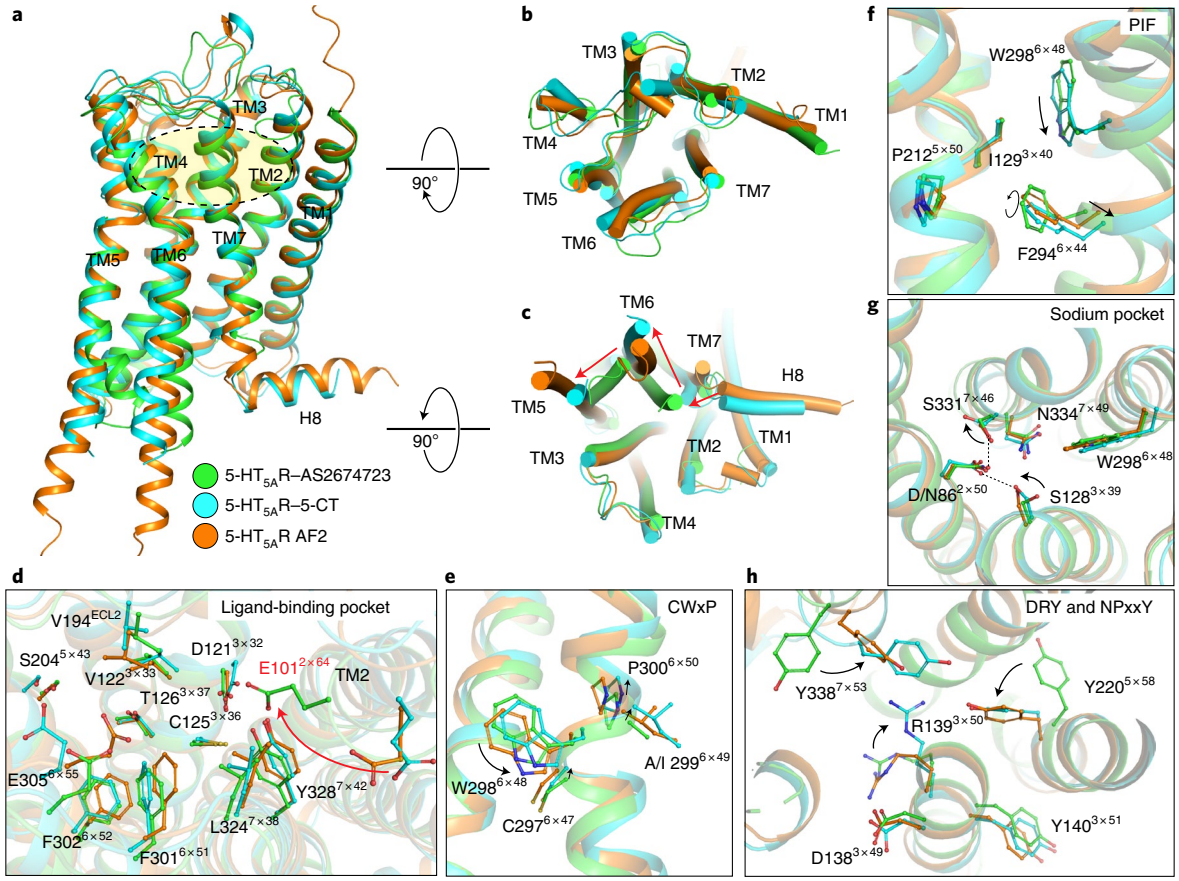

Fig. 5 | Activation of 5-HT$_{5A}$R. Structural comparison of the inactive state 5-HT$_{5A}$R structure, the active state 5-HT$_{5A}$R structure and the prediction 5-HT$_{5A}$R structure from the AlphaFold2 server. **a**, Side view. The ligand-binding pocket is indicated by a yellow shaded oval. **b**, Extracellular view. **c**, Intracellular view. The displacement directions of TM5, TM6 and TM7 are indicated by red arrows. **d**, Ligand-binding pocket. The rotation of E101 from the active state to the inactive state is indicated by a red arrow. **e**, The CWxP motif. **f**, The PIF motif. A299 and I299 are from inactive and active state structures at position 6×49, respectively. **g**, The sodium-binding site. N86 and D86 are from inactive and active state structures at position 2×50, respectively. Hydrogen bonds are indicated by black dashed lines. **h**, DRY and NPxxY motifs. Conformational changes from the inactive state to the active state are indicated by black arrows.

bind in a hydrophobic cavity formed by residues I143$^{3\times54}$, I223$^{5\times61}$, A227$^{5\times65}$, M286$^{6\times36}$ and V287$^{6\times37}$ of 5-HT$_{5A}$R (Fig. 4c). Surprisingly, unlike the strong π–cation interaction between R$^{6\times29}$ and Y$^{H5.26}$ in 5-HT$_1$R–G protein structures, there is a lysine instead of an arginine in 5-HT$_{5A}$R at position 6×29 and it does not form interactions with Y225$^{H5.26}$. Consistent with this, both K279$^{6\times29}$ and Y225$^{H5.26}$ show poor density maps in 5-HT$_{5A}$R–miniG$_o$ structures (Extended Data Fig. 3i). On the ICL2 side, residue M147$^{34\times51}$ inserts into the hydrophobic pocket formed by the α5 helix and the αN helix junction of miniG$_o$ (Fig. 4d). In the following mutagenesis study, S142$^{3\times53}$A and M147$^{34\times51}$A mutations showed no effect or slight effect on G$_{i1}$ activation; R230$^{5\times68}$A and M286$^{6\times36}$A mutations moderately affected signaling; I143$^{3\times54}$A, I223$^{5\times61}$A, R282$^{6\times32}$A and N342$^{8\times47}$A mutations dramatically reduced G$_{i1}$ activation; and R139$^{3\times50}$, R154$^{4\times38}$ and V287$^{6\times37}$ mutations abolished G$_{i1}$ activation (Fig. 4e). Moreover, we found that all the mutations of arginines in the cavity affected G$_{i1}$ activation, which indicated that a positively charged environment was important for G$_{i1}$ signaling activity (Extended Data Fig. 3k).

Intriguingly, although M147$^{34\times51}$ of ICL2 makes extensive hydrophobic interactions with the miniG$_o$ protein, the M147$^{34\times51}$A mutation does not alter G$_{i1}$ signaling activation (Fig. 4c,d). Therefore, sequence alignment of ICL2 loops of 5-HT receptors was performed, and we found that the residue H146$^{34\times50}$, adjacent to M147$^{34\times51}$, rendered 5-HT$_{5A}$R unique compared to the other 5-HT receptors, as it was an alanine or proline in other members at position 34×50 (Extended Data Fig. 6b). Accordingly, to explore the roles of H146$^{34\times50}$ in the stability of the 5-HT$_{5A}$R–G$_i$ complex, we carried out the miniG$_i$-recruitment assay[24]. Surprisingly, wild-type (WT) 5-HT$_{5A}$R was unable to efficiently recruit miniG$_i$ when stimulated with the full agonist 5-CT, whereas both mutations H146$^{34\times50}$A and H146$^{34\times50}$P could dramatically improve the miniG$_i$-recruitment ability (Fig. 4f). Therefore, the mutation corresponding to H146$^{34\times50}$P was also introduced into the construct for active state structure determination as mentioned above. Structural comparison of the inactive and active state 5-HT$_{5A}$R structures showed that H146$^{34\times50}$, a positively charged aromatic residue, could not fit into the hydrophobic groove formed by I215$^{H5.15}$ and I216$^{H5.16}$ as did proline or alanine, which might induce instability of the complex (Fig. 4d). Based on the mutants with H146$^{34\times50}$A or H146$^{34\times50}$P, extra point mutations, corresponding to M147$^{34\times51}$L, M147$^{34\times51}$V or M147$^{34\times51}$A, were introduced to examine the role of M147$^{34\times51}$ in G protein complex assembly and 5-HT$_{5A}$R signaling. Compared with the two single mutations H146$^{34\times50}$A and H146$^{34\times50}$P, the P$^{34\times50}$L$^{34\times51}$ mutation (short for the double mutation H146$^{34\times50}$P and M147$^{34\times51}$L, similarly below) slightly enhanced recruitment, A$^{34\times50}$V$^{34\times51}$ and P$^{34\times50}$V$^{34\times51}$ mutations dramatically reduced recruitment and mutants with A$^{34\times50}$A$^{34\times51}$ and P$^{34\times50}$A$^{34\times51}$ could not recruit miniG$_i$ as the WT did (Fig. 4f). By contrast, the results of the same mutants in the

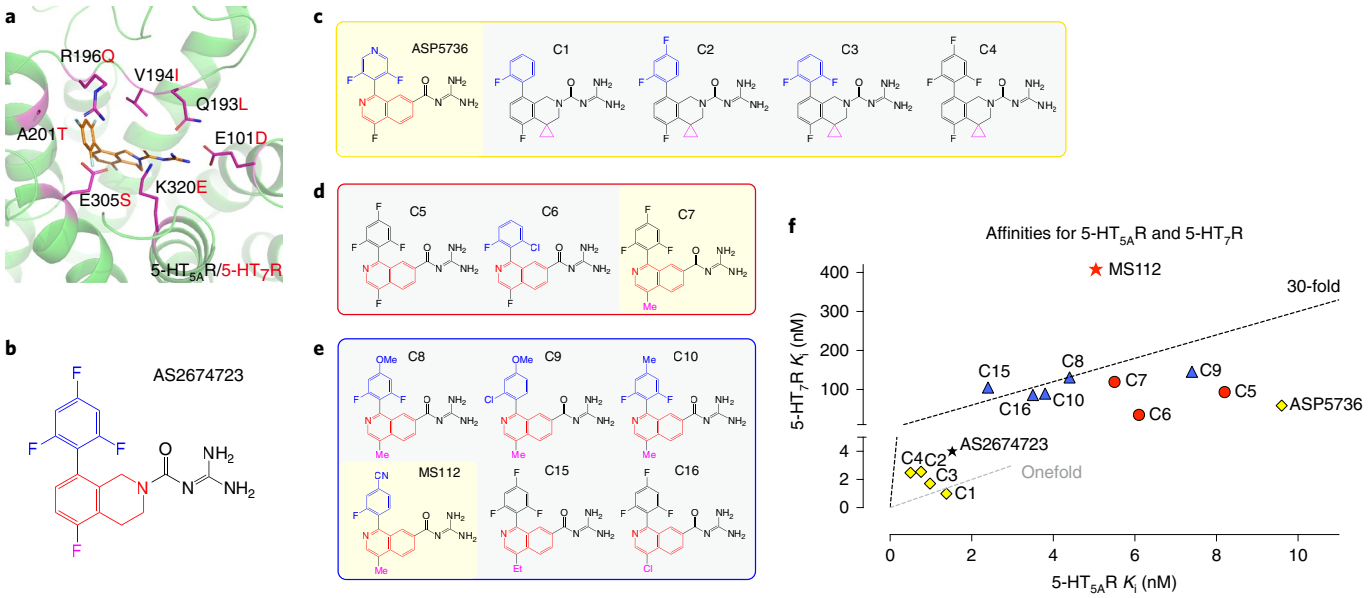

Fig. 6 | Selective antagonist development of 5-HT$_{5A}$R. a, Distribution of the residues of 5-HT$_{5A}$R interacting with AS2674723 that differ from those of 5-HT$_7$R in the 5-HT$_{5A}$R–AS2674723 structure. The different residues are shown as a stick model and are colored in magenta. The residues of 5-HT$_{5A}$R and 5-HT$_7$R are labeled in black and red, respectively. **b**, Chemical structure of the compound AS2674723. The trifluorophenyl ring binding in EBP2, the tetrahydroisoquinoline ring in the orthosteric pocket and the fluorine atom in the lower pocket are colored in blue, red and pink, respectively. **c**–**e**, Chemical structures of the first (**c**), second (**d**) and third (**e**) rounds of SAR-designed compounds. The variations from AS2674723 in different moieties are colored with the corresponding color used in **b**. Also, the best candidate compound in each round is highlighted in a shaded yellow box. Et, ethyl; Me, methyl. **f**, Binding affinities of the SAR-designed compounds for 5-HT$_{5A}$R and 5-HT$_{7A}$R. The compounds from the first, second and third rounds of SAR optimization are colored in yellow, red and blue, respectively. The starting compound AS2674723 and the featured compound MS112 are shown as black and red asterisks, respectively. All chemical structures of the ligands were illustrated with ChemDraw (20.0). See Supplementary Tables 7–10 for fitted parameter values that represent mean ± s.e.m. of $n = 3$ biological replicates.

G_{i1}-activation assay did not show significant differences between the WT and mutant 5-HT$_{5A}$Rs for either potency or efficacy (Fig. 4g). Together, these data show that the M147$^{34\times51}$ mutation was critical for the stability of the receptor–G protein complex but did not play an important role in the activation of G_i protein signaling.

Structural features of 5-HT$_{5A}$R activation. As we determined the structures of both inactive and active state 5-HT$_{5A}$Rs, a structural comparison was performed to investigate the molecular mechanism for 5-HT$_{5A}$R activation. Consistent with the previously reported GPCR–G protein complexes[23,25,26], the intracellular end of TM6 underwent the largest displacement and was tilted outward by 14.0 Å (Cα of E277$^{6\times27}$), while TM7 shifted inward by 3.2 Å (Cα of Y338$^{7\times53}$) during activation of 5-HT$_{5A}$R coupling the G protein (Fig. 5a–c). As TM5 forms a kink at the intracellular end in the inactive state, the movement direction is perpendicular to the TM6 segments and the distance is 7.2 Å (Cα of K228$^{5\times66}$) (Fig. 5c).

Accompanied by the helical movements, the microswitches also undergo extensive conformational changes. The W298$^{6\times48}$ residue of the CWxP motif rotates downward and pushes against residue F294$^{6\times44}$ of the PIF motif, causing it to move out by 2 Å (Cα) and causing the plane of its phenyl ring to rotate by 60° (ref. [27]) (Fig. 5e,f). In the sodium-binding site, as a result of the rotamer state changing of S128$^{3\times39}$ and S331$^{7\times46}$, the hydrogen bond between N86$^{2\times50}$ and S331$^{7\times46}$ is broken and reformed between D86$^{2\times50}$ and S128$^{3\times39}$, thus leading to the downstream helical movements[28–30] (Fig. 5g). In agreement with our prediction, the D86$^{2\times50}$N mutation stabilized the inactive state in the low-to-medium salt conditions used for crystallization[29]. Moreover, the side chains of R139$^{3\times50}$ in the DRY motif, Y338$^{7\times53}$ in the NPxxY motif and a conserved tyrosine Y338$^{7\times53}$ are also rearranged upon 5-HT$_{5A}$R activation (Fig. 5h).

We also explored the 5-HT$_{5A}$R structure model from the AlphaFold2 server[31] (referred to as the AF2 structure) and compared it with our inactive and active state structures. In comparison with the inactive structure, TM6 of the AF2 structure displaces outward and TM5 also does not form a kink (Fig. 5a–c). However, the outward movement of TM6 in the AF2 structure is less than in the active structure, which indicates that the AF2 structure may represent an intermediate state of 5-HT$_{5A}$R (Fig. 5c). In the orthosteric binding pocket of the AF2 structure, the E305$^{6\times55}$ residue rotates inside, V194^{ECL2} shifts downward and F301$^{6\times51}$ and F302$^{6\times52}$ move inward to the pocket, which results in a relatively shrunken pocket (Fig. 5d). Among the microswitches, the AF2 structure largely adopts the active conformation, except that R139$^{3\times50}$ in the DRY motif and S331$^{7\times46}$ in the sodium pocket are in the inactive conformation (Fig. 5e–h). As the 5-HT$_{5A}$R structure modeled by the AlphaFold2 server is ligand free, this model might represent the apo state of 5-HT$_{5A}$R and thus, together with our inactive and active state structures, could provide a more comprehensive understanding of 5-HT$_{5A}$R activation.

Structure-guided design of a selective 5-HT$_{5A}$R antagonist. As described above, compound AS2674723 has six off-target receptors, of which 5-HT$_7$R is the main one, among the aminergic receptors (Extended Data Fig. 5a). To guide selectivity optimization, we aligned the residues of 5-HT$_{5A}$R involved in binding AS2674723 with the corresponding residues of 5-HT$_7$R and mapped the unconserved residues in the 5-HT$_{5A}$R–AS2674723 structure (Fig. 6a and Extended Data Fig. 6a). As expected, the pocket residues of 5-HT$_{5A}$R and 5-HT$_7$R are highly similar with an overall similarity of 83% over 18 residues. In particular, two critical residues, E101$^{2\times64}$ and L324$^{7\times38}$, which are vital for 5-HT$_{5A}$R selectivity of AS2674723,

are highly conserved in 5-HT$_7$R (Extended Data Fig. 6a). Of the residues that do differ, all are located in the upper pocket (EBP2); thus, modifying the substitutions on the phenyl ring might increase the selectivity for 5-HT$_7$R (Fig. 6a,b).

In the first round of testing, we selected four compounds with high affinity for 5-HT$_{5A}$R from the patent literature[32] with varied fluorine substitutions on the upper phenyl ring and a cyclopropyl ring on the tetrahydroisoquinoline ring (Fig. 6c). We also selected the compound ASP5736, an AS2674723 analog with an isoquinoline core, for evaluation due to its better selectivity over other 5-HT receptors[8] (Fig. 6c). Our results indicated that four cyclopropyl-substituted tetrahydroisoquinoline ring derivates (C1, C2, C3 and C4) had improved affinities for 5-HT$_{5A}$R as well as other off-target receptors, resulting in overall decreased selectivity compared to AS2674723 (Fig. 6f and Supplementary Table 7). Moreover, our results did suggest a better selectivity of ASP5736 over 5-HT$_7$R (from 2.6-fold to 4.8-fold) and other receptors, albeit with a weaker binding affinity for 5-HT$_{5A}$R (10.7 nM) as compared to AS2674723 (1.5 nM) (Fig. 6f and Supplementary Table 7). Accordingly, we selected 16 analogs of ASP5736 from patent US 8,853,242 B2 (ref. [33]) to explore the effect of the upper pyridinyl moiety and the isoquinoline core region on selectivity (Extended Data Fig. 8a). To bias toward high affinities for 5-HT$_{5A}$R first, we used structure-based free-energy perturbation (FEP)[34] with the program FEP+ (ref. [35]) to evaluate differences in affinity between the designed compounds and the starting compound. Based on the FEP predictions, the top three scoring analogs were synthesized and tested (Fig. 6d and Extended Data Fig. 8a). Of these three analogs, the compound C7 displayed increased selectivity for 5-HT$_7$R (from 4.8-fold to 21.7-fold) and other off-target receptors compared to ASP5736 (Fig. 6f and Supplementary Table 8). The chemical structure of C7 features a methyl-substituted isoquinoline core with an upper trifluorophenyl ring (Fig. 6d).

To further improve the selectivity of C7, we explored directed substitutions on the upper phenyl ring and more substituent groups on the isoquinoline core. In total, we selected nine compounds from the patent US 8,853,242 B2 (ref. [33]) and designed 14 new compounds (Extended Data Fig. 8b). Based on the FEP analysis, ten compounds were selected for synthesis and biological evaluation. Of these, six compounds demonstrated good selectivity for 5-HT$_7$R (>20-fold; Fig. 6e,f and Supplementary Table 9). Notably, the new compound MS112, introducing a cyano group on the upper phenyl moiety and keeping the methyl group on the isoquinoline ring, maintained a high affinity for 5-HT$_{5A}$R (5.0 nM) with improved selectivity for 5-HT$_7$R (82.6-fold) and other tested aminergic receptors (more than 73.5-fold; 5-HT$_{1A}$R, 5-HT$_{1B}$R, 5-HT$_{1D}$R, α_{2A}AR and α_{2C}AR) (Fig. 6f and Supplementary Table 10). Also, MS112 still displayed the same level of antagonist activity as compounds ASP5736 and AS2674723 (Extended Data Fig. 9a,b).

We sought to evaluate the FEP predictions quantitatively, as the method may be broadly useful for ligand discovery for GPCRs. Accordingly, we analyzed the correlations between the $\Delta\Delta G$ values predicted by the FEP ($\Delta\Delta G_{FEP}$) and those calculated from the experimental results ($\Delta\Delta G_{exp}$). For three compounds (C5, C6 and C7) in the second round of optimization, their $\Delta\Delta G_{FEP}$ and $\Delta\Delta G_{exp}$ values were significantly correlated, with differences lower than fivefold (Extended Data Fig. 9c). In the last round of optimization, according to the FEP-predicted $\Delta\Delta G$ values, ten compounds could be classified into three classes: those with better ($\Delta\Delta G_{FEP} < -0.5$ kcal mol^{-1}; C16), similar ($0 < \Delta\Delta G_{FEP} < 0.5$ kcal mol^{-1}; C8, C9, C10, MS112, C12, C13 and C15) and worse ($\Delta\Delta G_{FEP} > 2.0$ kcal mol^{-1}; C11 and C14) potencies as compared to the lead compound C7 (Extended Data Fig. 8b). On experimental testing, compound C16 was found to display a potency quite similar to that of compound C7, with a $\Delta\Delta G_{exp}$ value of 0.01 kcal mol^{-1}. (Extended Data Fig. 9d). In the similar-potency class, six compounds displayed $\Delta\Delta G_{exp}$ values within 0.5 kcal mol^{-1}, with the exception of C13, with a $\Delta\Delta G_{exp}$ value of 1.1 kcal mol^{-1}. Finally, the $\Delta\Delta G_{exp}$ values of C11 and C14 were 0.7 kcal mol^{-1} and 0.3 kcal mol^{-1}, which were again off by fourfold and eightfold from their $\Delta\Delta G_{FEP}$ values, respectively (Extended Data Fig. 9d). Thus, quantitatively, the correlation between the predicted and measured affinity changes was modest. However, by less stringent qualitative criteria, the predictions were more accurate: molecules predicted to have improved affinity did maintain affinity and those predicted to be relatively unchanged typically only changed modestly, while molecules predicted to bind worse did bind worse. Whereas the field continues to strive for chemical accuracy (±1 kcal mol^{-1} root-mean-square error in predicted versus measured energies), even qualitative correlation between prediction and experiment is more than helpful in ligand optimization. This study supports the use of this technique in structure–activity relationship (SAR) campaigns for optimization of affinity and selectivity for GPCR ligands.

Discussion

In this paper, we determined the structure of the inactive state 5-HT$_{5A}$R stabilized by the antagonist AS2674723 and three agonist-activated structures coupled to its canonical transducer G$_o$ in complex with a partial agonist lisuride and two full agonists, 5-CT and methylergometrine. These structures provided molecular insights into ligand-binding modes of 5-HT$_{5A}$R and illuminated the selectivities of AS2674723 and 5-CT. Additionally, several structural features of 5-HT$_{5A}$R unique from those of other 5-HT receptors were revealed, including a bending TM4 and an unexpected kinked TM5 at the intracellular side. Together with the mutagenesis and functional studies, key determinants essential for agonist actions and receptor–G$_o$ coupling were also identified. Finally, based on the high-resolution structure and combined with FEP and SAR optimization, we obtained a new and highly selective 5-HT$_{5A}$R ligand with nanomolar affinity, which will be a powerful probe to investigate this understudied receptor. In conclusion, these observations have wide implications for the mechanistic understanding of 5-HT$_{5A}$R signaling and drug discovery.

Online content

Any methods, additional references, Nature Research reporting summaries, source data, extended data, supplementary information, acknowledgements, peer review information; details of author contributions and competing interests; and statements of data and code availability are available at https://doi.org/10.1038/s41594-022-00796-6.

Received: 19 January 2022; Accepted: 26 May 2022;
Published online: 14 July 2022

References

1. Barnes, N. M. et al. International Union of Basic and Clinical Pharmacology. CX. Classification of receptors for 5-hydroxytryptamine; pharmacology and function. *Pharmacol. Rev.* **73**, 310–520 (2021).
2. Berger, M., Gray, J. A. & Roth, B. L. The expanded biology of serotonin. *Annu. Rev. Med.* **60**, 355–366 (2009).
3. Grailhe, R. et al. Increased exploratory activity and altered response to LSD in mice lacking the 5-HT$_{5A}$ receptor. *Neuron* **22**, 581–591 (1999).
4. Pierce, P. A., Xie, G. X., Levine, J. D. & Peroutka, S. J. 5-Hydroxytryptamine receptor subtype messenger RNAs in rat peripheral sensory and sympathetic ganglia: a polymerase chain reaction study. *Neuroscience* **70**, 553–559 (1996).
5. Sagi, Y. et al. Emergence of 5-HT5A signaling in parvalbumin neurons mediates delayed antidepressant action. *Mol. Psychiatry* **25**, 1191–1201 (2020).
6. Pasqualetti, M. et al. Distribution of the 5-HT$_{5A}$ serotonin receptor mRNA in the human brain. *Brain Res. Mol. Brain Res.* **56**, 1–8 (1998).
7. Corbett, D. F. et al. Discovery of a potent and selective 5-HT$_{5A}$ receptor antagonist by high-throughput chemistry. *Bioorg. Med. Chem. Lett.* **15**, 4014–4018 (2005).
8. Yamazaki, M., Okabe, M., Yamamoto, N., Yarimizu, J. & Harada, K. Novel 5-HT$_{5A}$ receptor antagonists ameliorate scopolamine-induced working memory deficit in mice and reference memory impairment in aged rats. *J. Pharmacol. Sci.* **127**, 362–369 (2015).

9. Yamazaki, M. et al. ASP5736, a novel 5-HT_{5A} receptor antagonist, ameliorates positive symptoms and cognitive impairment in animal models of schizophrenia. *Eur. Neuropsychopharmacol.* **24**, 1698–1708 (2014).
10. Levit Kaplan, A. et al. Structure-based design of a chemical probe set for the 5-HT_{5A} serotonin receptor. *J. Med. Chem.* **65**, 4201–4217 (2022).
11. Erlander, M. G. et al. Two members of a distinct subfamily of 5-hydroxytryptamine receptors differentially expressed in rat brain. *Proc. Natl Acad. Sci. USA* **90**, 3452–3456 (1993).
12. Rees, S. et al. Cloning and characterisation of the human 5-HT_{5A} serotonin receptor. *FEBS Lett.* **355**, 242–246 (1994).
13. Francken, B. J., Jurzak, M., Vanhauwe, J. F., Luyten, W. H. & Leysen, J. E. The human 5-HT_{5A} receptor couples to G_i/G_o proteins and inhibits adenylate cyclase in HEK 293 cells. *Eur. J. Pharmacol.* **361**, 299–309 (1998).
14. Chun, E. et al. Fusion partner toolchest for the stabilization and crystallization of G protein-coupled receptors. *Structure* **20**, 967–976 (2012).
15. Isberg, V. et al. Generic GPCR residue numbers—aligning topology maps while minding the gaps. *Trends Pharmacol. Sci.* **36**, 22–31 (2015).
16. Popov, P. et al. Computational design of thermostabilizing point mutations for G protein-coupled receptors. *eLife* **7**, e34729 (2018).
17. Olsen, R. H. J. et al. TRUPATH, an open-source biosensor platform for interrogating the GPCR transducerome. *Nat. Chem. Biol.* **16**, 841–849 (2020).
18. Garcia-Nafria, J., Nehme, R., Edwards, P. C. & Tate, C. G. Cryo-EM structure of the serotonin 5-HT_{1B} receptor coupled to heterotrimeric G_o. *Nature* **558**, 620–623 (2018).
19. Duan, J. et al. Cryo-EM structure of an activated VIP1 receptor–G protein complex revealed by a NanoBiT tethering strategy. *Nat. Commun.* **11**, 4121 (2020).
20. Xu, P. et al. Structural insights into the lipid and ligand regulation of serotonin receptors. *Nature* **592**, 469–473 (2021).
21. Bach, T. et al. $5HT_{4(a)}$ and 5-$HT_{4(b)}$ receptors have nearly identical pharmacology and are both expressed in human atrium and ventricle. *Naunyn Schmiedebergs Arch. Pharmacol.* **363**, 146–160 (2001).
22. Grailhe, R., Grabtree, G. W. & Hen, R. Human 5-HT_5 receptors: the 5-HT_{5A} receptor is functional but the 5-HT_{5B} receptor was lost during mammalian evolution. *Eur. J. Pharmacol.* **418**, 157–167 (2001).
23. Kim, K. et al. Structure of a hallucinogen-activated G_q-coupled 5-HT_{2A} serotonin receptor. *Cell* **182**, 1574–1588 (2020).
24. Wan, Q. et al. Mini G protein probes for active G protein-coupled receptors (GPCRs) in live cells. *J. Biol. Chem.* **293**, 7466–7473 (2018).
25. Wacker, D., Stevens, R. C. & Roth, B. L. How ligands illuminate GPCR molecular pharmacology. *Cell* **170**, 414–427 (2017).
26. Weis, W. I. & Kobilka, B. K. The molecular basis of G protein-coupled receptor activation. *Annu. Rev. Biochem.* **87**, 897–919 (2018).
27. Katritch, V., Cherezov, V. & Stevens, R. C. Structure–function of the G protein-coupled receptor superfamily. *Annu. Rev. Pharmacol. Toxicol.* **53**, 531–556 (2013).
28. Che, T. et al. Structure of the nanobody-stabilized active state of the κ opioid receptor. *Cell* **172**, 55–67 (2018).
29. White, K. L. et al. Structural connection between activation microswitch and allosteric sodium site in GPCR signaling. *Structure* **26**, 259–269 (2018).
30. Katritch, V. et al. Allosteric sodium in class A GPCR signaling. *Trends Biochem. Sci.* **39**, 233–244 (2014).
31. Jumper, J. et al. Highly accurate protein structure prediction with AlphaFold. *Nature* **596**, 583–589 (2021).
32. Hamaguchi, W. et al. Tetrahydroisoquinoline derivative. US patent 8,962,612 B2 (2015).
33. Kinoyama, I. et al. Nitrogenous-ring acylguanidine derivative. US patent 8,853,242 B2 (2014).
34. Cournia, Z., Allen, B. & Sherman, W. Relative binding free energy calculations in drug discovery: recent advances and practical considerations. *J. Chem. Inf. Model.* **57**, 2911–2937 (2017).
35. Schrödinger Release 2020-4: FEP+ (Schrödinger, 2021).

Methods

Generation of 5-HT$_{5A}$R constructs for crystallization and cryo-electron microscopy. For crystallization, the human *HTR5A* gene (UniProt ID P47898) was cloned into a modified pFastBac1 vector (Invitrogen) containing sequences for a hemagglutinin signal peptide followed by Flag tag, His$_{10}$ tag and a TEV protease site at the N terminus. The construct was further optimized by fusing the sequence for the protein PGS (UniProt ID Q9V2J8) to that for the third intracellular loop at V231 and E277 encoded in the *HTR5A* gene, truncating the sequence for N-terminal residues 1–22 and introducing two thermostabilizing mutations (corresponding to D86$^{2\times50}$N and I229$^{6\times49}$A).

For cryo-EM, to facilitate protein expression and subsequent purification, thermostabilized apocytochrome b562RIL (BRIL) and an HRV3C protease site were introduced at the N terminus and an LgBiT fragment was introduced at the C terminus of the receptor, respectively. For the miniG$_o$ heterotrimeric complex, we replaced the sequence for miniG$_{sqiN}$ with the sequence for our miniG$_o$ in the pFastBac dual expression system, which has been used for the structural determination of the 5-HT$_{2A}$R–G$_q$ complex[23]. A HiBiT fragment was fused to the C terminus of the β subunit to enhance complex formation with the receptor.

Expression of 5-HT$_{5A}$R-crystallization and -cryo-electron microscopy constructs. The Bac-to-Bac baculovirus expression system (Invitrogen) was used to generate recombinant baculovirus for protein expression. Before infection, viral titers were determined by flow cytometric analysis of cells stained with anti-gp64–PE antibody (Expression Systems, 97-201, diluted 1:200 in PBS). For inactive state 5-HT$_{5A}$R, expression of 5-HT$_{5A}$R was carried out by infection of Sf9 cells (Expression Systems, 94-001S) at a cell density of 2×10^6 cells per ml in ESF921 medium (Expression Systems, 96-001) with P1 virus at a multiplicity of infection of 3. Cells were collected by centrifugation at 48 h after infection, washed with TN buffer (20 mM Tris-Cl, 100 mM NaCl, pH 7.5) and stored at −80 °C until use. For the 5-HT$_{5A}$R–miniG$_o$ complex, 5-HT$_{5A}$R, miniG$_o$-Gβ1γ2 and scFv16 were coexpressed by infecting Sf9 cells at a density of 2×10^6 cells per ml with P1 baculovirus at a multiplicity of infection ratio of 3:1:1, respectively. Cells were collected by centrifugation 48 h after infection and stored at −80 °C for future use.

Purification of inactive state 5-HT$_{5A}$R. Purification of inactive state 5-HT$_{5A}$R was performed similarly to the purification of inactive state 5-HT$_{2A}$R[23]. Thawed insect cell membranes were disrupted in a hypotonic buffer containing 10 mM HEPES (pH 7.5), 10 mM $MgCl_2$, 20 mM KCl and protease inhibitors containing 500 µM AEBSF, 1 µM E-64, 1 µM leupeptin and 0.15 µM aprotinin. Subsequently, soluble and membrane-associated proteins were removed in a high osmotic buffer containing 10 mM HEPES (pH 7.5), 1 M NaCl, 10 mM $MgCl_2$ and 20 mM KCl. Purified membranes were incubated in the presence of 10 µM AS2674723 and protease inhibitor cocktail at 4 °C for 2 h. The membranes were incubated with 2.0 mg ml^{-1} iodoacetamide (Sigma, I1149) for 30 min and were solubilized in buffer containing 50 mM HEPES (pH 7.5), 1% (wt/vol) *n*-dodecyl-β-D-maltopyranoside (DDM, Anatrace, D310), 0.2% (wt/vol) cholesterol hemisuccinate (CHS, Sigma, C6512) and 150 mM NaCl at 4 °C for 2 h. Solubilized 5-HT$_{5A}$R was isolated by ultracentrifugation at 185,000*g* and 4 °C for 50 min, and then samples were incubated at 4 °C overnight with TALON IMAC resin (Clontech, 635507), 800 mM NaCl and 20 mM imidazole as the final buffer concentration. The resin was washed with ten column volumes of washing buffer I containing 50 mM HEPES (pH 7.5), 0.1% (wt/vol) DDM, 0.02% (wt/vol) CHS, 800 mM NaCl, 10% (vol/vol) glycerol, 20 mM imidazole and 1 µM AS2674723 and ten column volumes of washing buffer II containing 50 mM HEPES (pH 7.5), 0.05% (wt/vol) DDM, 0.01% (wt/vol) CHS, 500 mM NaCl, 10% (vol/vol) glycerol and 1 µM AS2674723 without imidazole. The protein was eluted using three column volumes of elution buffer containing 50 mM HEPES (pH 7.5), 0.05% (wt/vol) DDM, 0.01% (wt/vol) CHS, 500 mM NaCl, 10% (vol/vol) glycerol, 250 mM imidazole and 10 µM AS2674723, concentrated in a Vivaspin 20 concentrator with a molecular weight cutoff of 100 kDa (Sartorius Stedim, VS2042) to 500 µl and applied to PD MiniTrap G-25 columns (GE Healthcare, 28-9180-07) to remove imidazole. The fusion and 10× His tag were removed by adding His-tagged PreScission protease (GenScript, Z0392-500) and incubating overnight at 4 °C. The protease, cleaved His tag and uncleaved protein were trapped with equilibrated TALON IMAC resin, and the flow-through was collected. The 5-HT$_{5A}$R–AS2674723 complex was concentrated to around 30 mg ml^{-1} using a Vivaspin 500 centrifuge concentrator with a molecular weight cutoff of 100 kDa (Sartorius Stedim, VS0142). Protein purity and monodispersity were tested with an analytical size-exclusion chromatography column (Sepax Scientific, SRT-300) and Ultimate 3000 UHPLC systems (Thermo Scientific).

Lipidic cubic phase crystallization. The purified 5-HT$_{5A}$R protein in complex with AS2674723 was screened for crystallization in lipidic cubic phase (LCP) with mixed molten lipid (90% (wt/vol) monoolein and 10% (wt/vol) cholesterol) at a protein:lipid ratio of 1:1.5 (vol/vol) using a mechanical syringe mixer[23,36]. Crystallization was performed with 96-well glass sandwich plates (Marienfeld, 0890003) in 50-nl LCP drops that were dispersed from a 10-µl gas-tight pipette (Hamilton) using a handheld dispenser (Art Robbins Instruments) and overlaid with 1 µl precipitant solution. After optimization, crystals were obtained in several conditions: 0.1 M sodium chloride, 0.1 M lithium sulfate, 0.1 M DL-malic acid, pH 5.9, 30% (vol/vol) PEG 400; 0.2 M sodium chloride, 0.4 M lithium sulfate, 0.1 M sodium citrate, pH 5.0, 30% (vol/vol) PEG MME 500; and 0.4 M potassium phosphate monobasic, 0.1 M Tris, pH 8.0, 30% (vol/vol) PEG 400. Crystals grew to a maximum size of ~30 mm × 20 mm × 20 mm within 2 weeks and were collected directly from the LCP plates using MiTeGen micromounts and stored in liquid nitrogen.

X-ray data collection, structure determination and refinement. Data collection was performed using JBluIce-EPICS data-acquisition software at the GM/CA-CAT (23-ID-D) beamline at the Advanced Photon Source of the Argonne National Laboratory using a 10–20-µm mini-beam at a wavelength of 1.0332 Å and a PILATUS3 6M detector. Crystals within the loops were located by diffraction using the automated rastering module of JBluIce-EPICS. Partial datasets (wedges of 5–10°) were collected from crystals exposed to the non-attenuated mini-beam for 0.2–0.3 s with 0.2–0.3° of oscillation per exposure; a 99.2% complete dataset at a resolution of 2.8 Å was obtained by indexing, integrating, scaling and merging partial datasets from 17 crystals using HKL-3000. Structure determination was performed by molecular replacement using the Phaser module in the Phenix suite. Two search models, one containing the PGS domain and one containing the receptor seven-helix bundle, were created using the structures of OX$_2$R (PDB 4S0V) and 5-HT$_{1B}$R–ergotamine (PDB 4IAR), respectively. Subsequent refinement was performed using the molecular replacement solution with rounds of phenix.refine with simulated annealing and REFMAC5 using translation, libration and screw-rotation parameters along with the overall setting for *B* factor refinement. Manual examination and rebuilding of refined coordinates were accomplished using Coot. The quality of the model was checked using the MolProbity server. The Ramachandran statistics analyzed using MolProbity are 93.9% favored, 6.1% allowed and 0.0% outliers for this structure. A summary of data collection and refinement statistics is reported in Table 1. The $2F_o - F_c$ maps imported into PyMOL were generated using the FFT program of the CCP4 suite. Figures were prepared in PyMOL (Schrödinger).

Receptor–G protein complex purification. Purification of active state 5-HT$_{5A}$R was performed similarly to the purification of the MRGPRX2–G$_q$–scFv16 complex[37]. The cell pellet expressing the 5-HT$_{5A}$R–miniG$_o$ complex was thawed on ice and incubated with a buffer containing 20 mM HEPES, pH 7.5, 50 mM NaCl, 1 mM $MgCl_2$, proteinase inhibitor and agonist (5-CT, lisuride or methylergometrine) at room temperature. After 1.5 h, the cell suspension was homogenized. Membranes were collected by centrifugation at 70,000*g* for 30 min using a Ti45 rotor (Beckman) and solubilized using 40 mM HEPES, pH 7.5, 100 mM NaCl, 5% (wt/vol) glycerol, 0.5% (wt/vol) lauryl maltose neopentyl glycol (LMNG, Anatrace, NG310) and 0.05% (wt/vol) CHS for 5 h at 4 °C. The solubilized proteins in the supernatants were isolated by ultracentrifugation at 160,000*g* for 30 min using a Ti70 rotor and then incubated overnight at 4 °C with TALON IMAC resin and 20 mM imidazole. The resin was collected the next day and washed with 25 column volumes of 20 mM HEPES, pH 7.5, 100 mM NaCl, 30 mM imidazole, 0.01% (wt/vol) LMNG, 0.001% (wt/vol) CHS and 5-HT$_{5A}$ agonist (5-CT, lisuride or methylergometrine). The protein was then eluted using the same buffer supplemented with 250 mM imidazole. Eluted protein was concentrated and subjected to size-exclusion chromatography on a Superdex 200 Increase 10/300 column (GE Healthcare, 289909944) that was pre-equilibrated with 20 mM HEPES, pH 7.5, 100 mM NaCl, 1 µM agonist, 0.00075% (wt/vol) LMNG, 0.00025 (wt/vol), glyco-diosgenin (Anatrace, GDN101) and 0.00075% (wt/vol) CHS. Peak fractions were collected and incubated with 15 µl His-tagged PreScission protease and 2 µl PNGase F (NEB, P0708S) at 4 °C overnight to remove the N-terminal BRIL and potential glycosylation. The protein was concentrated and further purified the next day by size-exclusion chromatography using the same buffer. Peak fractions were collected and concentrated to around 5 mg ml^{-1}.

Cryo-electron microscopy data collection, three-dimensional reconstitution, model building and refinement. Cryo-EM data collection and processing for the 5-HT$_{5A}$R–miniG$_o$ complex was performed following a published protocol[38]. The samples (3.2 µl) were applied to glow discharged Quantifoil R1.2/1.3 Au300 holey carbon grids (Ted Pella) individually and were flash frozen in a liquid ethane–propane (40:60) mixture using a Vitrobot Mark IV (FEI) set at 4 °C and 100% humidity with a blot time range from 2.5 to 5 s. Images were collected using a 200-keV Talos Artica with a Gatan K3 direct electron detector at a physical pixel size of 0.91 Å. Micrograph recorded movies were automatically collected using SerialEM with a multishot array[39]. Data were collected at an exposure dose rate of ~15 electrons per pixel per second as recorded from counting mode. Images were recorded for ~1.7–2.7 s in 60 subframes to give a total exposure dose of ~29–48 electrons per Å^2. Following manual inspection and curation of the micrographs, particles from each dataset were selected using the Blob particle picker, and initial two-dimensional classification yielded templates for subsequent template picking. After one round of two-dimensional classification and selection in cryoSPARC, a subset of the selected particles was used as a training set for Topaz, and the particles were repicked from the micrographs using Topaz[40] and subjected to two-dimensional classification and three-dimensional classification. The select classified picked particle coordinates from the three sets were next

merged, yielding a subset of unique particles that survived two-dimensional classification (that is, duplicates were removed with a radius of 75 pixels). All subsequent three-dimensional classification and refinement steps were performed with cryoSPARC[41,42]. Multiple rounds of multi-reference refinement resolved the final stack of particles that produced a map with a resolution reported in Table 2 (by FSC using the cutoff criterion of 0.143 Å)[43] after Global CTF refinement and post-processing including soft masking, *B* factor sharpening in cryoSPARC and filtering by local resolution[44] to generate the post-processed sharpened map. Alternative post-sharpening was performed on the two half-maps using DeepEMhancer[45]. For more details, see Table 2 and Extended Data Fig. 2.

Maps from DeepEMhancer were used for map building, refinement and subsequent structural interpretation. The 5-HT_{1B}R–miniG_o structure (PDB 6G79) was used as the initial model and docked into the cryo-EM map using Chimera[46], followed by iterative manual adjustment in Coot[47] and the 'phenix.real_space_refine' tool in Phenix[48]. Model statistics were validated using MolProbity[49]. Structural figures were prepared using Chimera or PyMOL (https://pymol.org/2/).

Bioluminescence resonance energy transfer (BRET1 and BRET2). To measure G protein recruitment (BRET1) of 5-HT_{5A}R, HEK293T cells (ATCC, CRL-11268) maintained in DMEM containing 10% (vol/vol) dialyzed FBS, 1 IU ml^{-1} penicillin G and 100 µg ml^{-1} streptomycin were passaged on 10-cm dishes and cotransfected using TransIT (Mirus Bio) at an approximate ratio of 1:3 to express WT or mutant 5-HT_{5A}R containing C-terminal *Renilla* luciferase (*R*luc) and Venus-tagged N-terminal miniG_i protein containing an N-terminal nuclear export signal, respectively[24]. After at least 24 h, transfected cells were plated in poly-lysine-coated 96-well white clear-bottom cell culture plates in plating medium (DMEM containing 1% (vol/vol) dialyzed FBS, 1 IU ml^{-1} penicillin G and 100 µg ml^{-1} streptomycin) at a density of 40,000 cells at 200 µl per well and incubated overnight. The following day, the medium was aspirated, and cells were washed once with 60 µl drug buffer (1× HBSS, 20 mM HEPES, pH 7.4). Next, 60 µl *R*luc substrate, coelenterazine h (Promega), was added at a final concentration of 5 µM, and drug stimulation was performed by adding 30 µl per well of a 3× drug dilution in drug-dilution buffer (1× HBSS, 20 mM HEPES, 0.3% (wt/vol) BSA, 0.03% (wt/vol) ascorbic acid, pH 7.4) and incubating at room temperature. After 10 min of incubation, plates were read for both luminescence at 485 nm and fluorescent eYFP emission at 530 nm for 1 s per well using a Mithras LB 940 reader (Berthold Technologies). The BRET ratio of eYFP/*R*luc per well was calculated and plotted as a function of drug concentration using GraphPad Prism 9.2 (GraphPad Software).

To measure 5-HT_{5A}-mediated G protein dissociation (BRET2), procedures were similar to those for 5-HT_{5A} recruitment, except that HEK293T cells were cotransfected at a 1:1:2:2 ratio of plasmids encoding G_{i1}-*R*luc, Gβ_1, GFP_2-Gγ_2 and 5-HT_{5A}R, respectively. G protein-dissociation BRET2 assays used 10 µl of the *R*luc substrate coelenterazine 400a (Nanolight, final concentration of 5 µM), and samples were incubated for 10 min and read for luminescence at 400 nm and fluorescent GFP_2 emission at 515 nm for 1 s per well using a Mithras LB 940 reader. The ratio of GFP_2/*R*luc per well was calculated and plotted as a function of drug concentration using GraphPad Prism 9.2 (GraphPad Software).

Radioligand-binding assays. Competitive binding assays were performed using membrane preparations from HEK293T cells transiently expressing WT or mutant 5-HT_{5A}R. Binding assays were set up in 96-well plates in the standard binding buffer (50 mM Tris, 0.1 mM EDTA, 10 mM $MgCl_2$, 0.1% BSA, 0.01% ascorbic acid, pH 7.40). For competition binding, 50 µl each of ^{3}H[LSD], drug solution (3×) and homogeneous membrane solution containing WT or mutant 5-HT_{5A}R were incubated in 96-well plates in the standard binding buffer. Reactions were incubated for 2 h at room temperature in the dark, terminated by rapid vacuum filtration onto chilled 0.3% PEI-soaked GF/A filters, followed by three quick washes with cold washing buffer (50 mM Tris-HCl, pH 7.40) and read. Results were analyzed using the equation 'one-site fit Ki' in GraphPad Prism 9.2.

FEP+ calculations. All calculations were carried out using version 2020-4 of the Schrödinger modeling suite[35]. The X-ray crystal structure of 5-HT_{5A}R–AS2674723 was prepared with the Protein Preparation Wizard with the default protocol, and protonation states of histidine, glutamate and aspartate residues were predicted by PROPKA[50] at pH 7.4. A membrane of pre-equilibrated (300 K) POPC lipids based on the OPM database alignment was added to the system together with SPC solvent. Counterions were added to neutralize the system with additional Na^+ and Cl^- ions added to a concentration of 0.15 mM. The MD systems were equilibrated for 100 ps of Brownian NVT at 10 K with restraints on all the solute's heavy atoms, followed by 100 ps of Brownian NPT at 50 K and 200 ps of NPγT at 50 K. Next, the system was heated from 100 K to 300 K over 300 ps of NPγT ensemble and gradual release of restraints. A final NVT unrestrained was run for 200 ps. The production runs were sampled for 50 ns of unrestrained NPγT ensemble at 298 K.

Glide SP docking with tight core constraint was used to align ligands to AS2674723 in the equilibrated system. Missing torsional parameters of ligands were added by fitting additional quantum mechanical calculations with Force Field Builder[51]. Two rounds of FEP were performed using FEP+ (ref. [52]). Only heavy atoms of the ligand were included in the REST region. A total of 12 λ windows were used for all calculations, and replica exchanges between neighboring λ windows were attempted every 1.2 ps.

The first perturbation map was built with ASP5736 as the reference compound and the default protocol. Three (C5, C6 and C7) of 16 compounds with predicted $\Delta\Delta G < -0.5$ kcal mol^{-1} were recommended for synthesis and testing. C7 emerged from the first-round FEP and was used as the reference compound for the second perturbation map. Allowing for free rotation of the benzene ring, isoquinoline was used as the custom core of the perturbation map. To test the FEP method prospectively, ten compounds were synthesized: C16 with predicted $\Delta\Delta G < -0.5$ kcal mol^{-1}; C8, C9, C10, C12, C13, MS112 and C15 with predicted $\Delta\Delta G < 0.5$ kcal mol^{-1}; C11 and C14 with predicted $\Delta\Delta G > 2$ kcal mol^{-1}.

For the calculations of the experimental $\Delta\Delta G$ values, we applied the equation $\Delta G = -RT\ln(K_i)$ based on the K_i affinities (M) of the compounds. In the equation, R is the gas constant (1.987×10^{-3} kcal K^{-1} mol^{-1}) and T is the temperature in Kelvin (here, it is 298.15 K).

Surface expression. Cell surface expression of WT and mutant 5-HT_{5A}Rs was measured using ELISA chemiluminescence[37]. In brief, 48 h after transfection, cells plated in white 384-well plates were fixed with 20 µl per well of 4% (vol/vol) paraformaldehyde for 10 min at room temperature. The cells were then washed twice with 40 µl PBS per well and then incubated with 20 µl per well of 5% (vol/vol) BSA in PBS for 1 h. Cells were incubated with an anti-Flag-horseradish peroxidase-conjugated antibody (Sigma-Aldrich, A8592) diluted 1:10,000 in 5% (vol/vol) BSA in PBS for 1 h at room temperature. After washing five times with 80 µl PBS per well, 20 µl per well of SuperSignal ELISA Pico Substrate (Thermo Fisher, 37070) was added for signal development, and luminescence was counted using a PHERAstar FSX (BMG LABTECH). The luminescence signal was analyzed in GraphPad Prism 9.2, and data were normalized to the signal of WT 5-HT_{5A}R.

Reporting summary. Further information on research design is available in the Nature Research Reporting Summary linked to this article.

Data availability

The structures of 5-HT_{5A}R–AS2674723, 5-HT_{5A}R–miniG_o–5-CT, 5-HT_{5A}R–miniG_o–lisuride and 5-HT_{5A}R–miniG_o–methylergometrine have been deposited in the PDB (EMDB) under accession codes 7UM4, 7UM5 (EMD-26597), 7UM6 (EMD-26598) and 7UM7 (EMD-26599). The cryo-EM micrographs of 5-HT_{5A}R–miniG_o–5-CT, 5-HT_{5A}R–miniG_o–lisuride and 5-HT_{5A}R–miniG_o–methylergometrine have been deposited in the EMPIAR database (https://www.ebi.ac.uk/empiar/) with accession numbers EMPIAR-11033, EMPIAR-11036 and EMPIAR-11039, respectively. Source data are provided with this paper.

References

36. Caffrey, M. & Cherezov, V. Crystallizing membrane proteins using lipidic mesophases. *Nat. Protoc.* **4**, 706–731 (2009).
37. Cao, C. et al. Structure, function and pharmacology of human itch GPCRs. *Nature* **600**, 170–175 (2021).
38. Peck, J. V., Fay, J. F. & Strauss, J. D. High-speed high-resolution data collection on a 200 keV cryo-TEM. *IUCrJ* **9**, 243–252 (2022).
39. Mastronarde, D. N. Automated electron microscope tomography using robust prediction of specimen movements. *J. Struct. Biol.* **152**, 36–51 (2005).
40. Bepler, T., Kelley, K., Noble, A. J. & Berger, B. Topaz-Denoise: general deep denoising models for cryoEM and cryoET. *Nat. Commun.* **11**, 5208 (2020).
41. Punjani, A., Rubinstein, J. L., Fleet, D. J. & Brubaker, M. A. cryoSPARC: algorithms for rapid unsupervised cryo-EM structure determination. *Nat. Methods* **14**, 290–296 (2017).
42. Punjani, A., Zhang, H. & Fleet, D. J. Non-uniform refinement: adaptive regularization improves single-particle cryo-EM reconstruction. *Nat. Methods* **17**, 1214–1221 (2020).
43. Rosenthal, P. B. & Henderson, R. Optimal determination of particle orientation, absolute hand, and contrast loss in single-particle electron cryomicroscopy. *J. Mol. Biol.* **333**, 721–745 (2003).
44. Heymann, J. B. & Belnap, D. M. Bsoft: image processing and molecular modeling for electron microscopy. *J. Struct. Biol.* **157**, 3–18 (2007).
45. Sanchez-Garcia, R. et al. DeepEMhancer: a deep learning solution for cryo-EM volume post-processing. *Commun. Biol.* **4**, 874 (2021).
46. Pettersen, E. F. et al. UCSF Chimera—a visualization system for exploratory research and analysis. *J. Comput. Chem.* **25**, 1605–1612 (2004).
47. Emsley, P. & Cowtan, K. Coot: model-building tools for molecular graphics. *Acta Crystallogr. D Biol. Crystallogr.* **60**, 2126–2132 (2004).
48. Adams, P. D. et al. PHENIX: a comprehensive Python-based system for macromolecular structure solution. *Acta Crystallogr. D Biol. Crystallogr.* **66**, 213–221 (2010).
49. Chen, V. B. et al. MolProbity: all-atom structure validation for macromolecular crystallography. *Acta Crystallogr. D Biol. Crystallogr.* **66**, 12–21 (2010).
50. Olsson, M. H., Sondergaard, C. R., Rostkowski, M. & Jensen, J. H. PROPKA3: consistent treatment of internal and surface residues in empirical pK_a predictions. *J. Chem. Theory Comput.* **7**, 525–537 (2011).

51. Harder, E. et al. OPLS3: a force field providing broad coverage of drug-like small molecules and proteins. *J. Chem. Theory Comput.* **12**, 281–296 (2016).
52. Abel, R., Wang, L., Harder, E. D., Berne, B. J. & Friesner, R. A. Advancing drug discovery through enhanced free energy calculations. *Acc. Chem. Res.* **50**, 1625–1632 (2017).

Acknowledgements

This work was supported by US National Institutes of Health grants RO1MH112205 and U24DK1169195 (to B.L.R.) and by R35GM122481 (to B.K.S.). This work also used the NMR spectrometer systems at Mount Sinai, acquired with funding from National Institutes of Health SIG grants 1S10OD025132 and 1S10OD028504 (to J.J.). We gratefully acknowledge M.J. Miley and the UNC macromolecular crystallization core for the use of their equipment for crystal collection and transport along with the UNC Flow Cytometry Core Facility. Both facilities are supported in part by a P30 CA016086 Cancer Center Core Support Grant to the UNC Lineberger Comprehensive Cancer Center. We also thank the staff of GM/CA@APS, which has been funded with federal funds from the National Cancer Institute (ACB-12002) and the National Institute of General Medical Sciences (AGM-12006). This research used resources of the Advanced Photon Source, a US Department of Energy Office of Science User Facility operated for the Department of Energy Office of Science by Argonne National Laboratory under contract no. DE-AC02-06CH11357. We thank J. Peck and J. Strauss of the UNC CryoEM Core Facility for their excellent technical assistance with this project. We are grateful to Schrödinger for the academic grant of FEP+ and multiple other tools in their software suite. The Titan X Pascal used for this research was kindly donated to J.F.F. by Nvidia.

Author contributions

S.Z. designed the experiments; performed cloning, expression, purification and preparation of the 5-HT_{5A}R–miniG_o complexes, model building and structure refinement in the cryo-EM study; performed purification of the inactive state 5-HT_{5A}R–AS2674723 complex and LCP crystallization, data collection and model building and refinement in the X-ray study; performed mutagenesis and functional studies; performed the binding assay and profiled SAR-designed compounds; and prepared the manuscript. H.C., J.L. and Y.X. performed the SAR study for selective compound development of 5-HT_{5A}R. C.Z. synthesized the AS2674723 compounds for the inactive state structure study. Y.Y. performed the FEP analysis. P.P. and V.K. performed computational predictions of the thermostabilizing point mutations. B.E.K., C.C. and K.K. assisted with protein expression. B.K.S. supervised the FEP analysis. J.J. supervised medicinal chemistry experiments. J.F.F. made the grids and collected and processed cryo-EM data. B.L.R. supervised the entire project, guided the structural and functional work and prepared the manuscript.

Competing interests

B.K.S. serves on the SAB of Schrödinger. The remaining authors declare no competing interests.

Additional information

Extended data is available for this paper at https://doi.org/10.1038/s41594-022-00796-6.

Supplementary information The online version contains supplementary material available at https://doi.org/10.1038/s41594-022-00796-6.

Correspondence and requests for materials should be addressed to Jonathan F. Fay or Bryan L. Roth.

Peer review information *Nature Structural and Molecular Biology* thanks Yunje Cho and the other, anonymous, reviewer(s) for their contribution to the peer review of this work. Primary Handling Editor: Florian Ullrich, in collaboration with the *Nature Structural & Molecular Biology* team. Peer reviewer reports are available.

Reprints and permissions information is available at www.nature.com/reprints.

a

	h5-HT1A	h5-HT1B	h5-HT1D	h5-HT1E	h5-HT1F	h5-HT2A	h5-HT2B	h5-HT2C	h5-HT4	h5-HT5A	h5-HT6	h5-HT7
h5-HT1A	-	35	34	33	32	17	19	19	24	26	18	22
h5-HT1B	50	-	54	42	41	20	20	19	23	29	18	24
h5-HT1D	48	68	-	42	42	20	19	21	23	29	20	23
h5-HT1E	47	55	55	-	53	20	19	22	25	28	20	24
h5-HT1F	47	55	57	68	-	19	18	22	24	28	19	24
h5-HT2A	32	34	37	34	34	-	35	45	20	19	21	22
h5-HT2B	31	35	35	33	36	49	-	36	20	17	19	19
h5-HT2C	32	35	37	35	37	57	54	-	21	20	21	19
h5-HT4	33	32	32	35	37	34	32	35	-	21	23	25
h5-HT5A	44	46	48	45	45	35	31	36	33	-	21	23
h5-HT6	29	31	33	32	32	36	34	36	37	34	-	21
h5-HT7	34	36	35	34	36	37	35	34	37	37	33	-

b

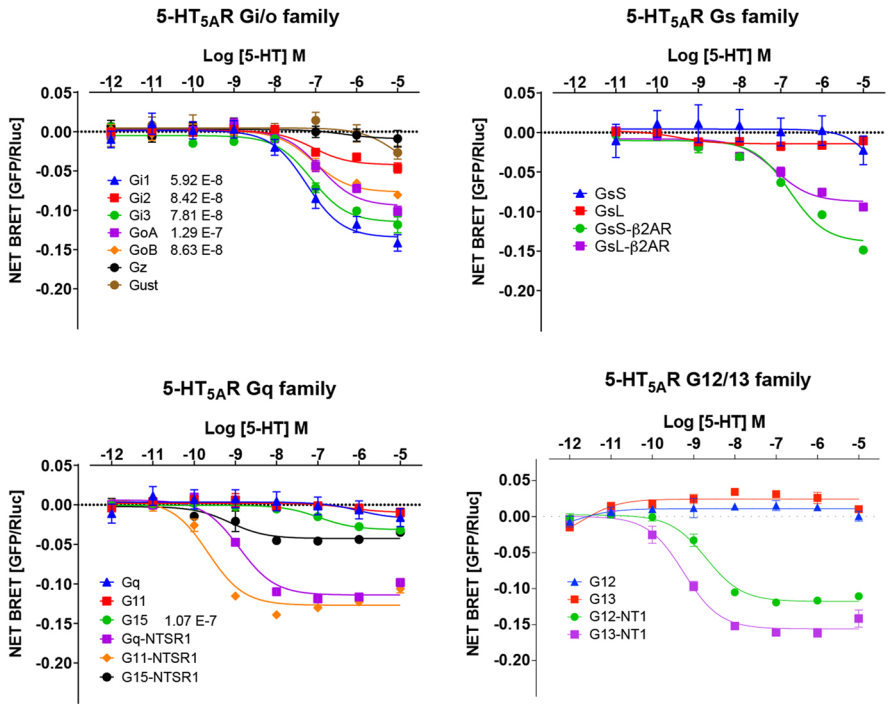

Extended Data Fig. 1 | Sequence alignment and transducerome profiling of 5-HT$_{5A}$R. a, Sequencing alignment matrix of the 12 GPCR members in the 5-HT receptor family. Similarities are shown on the lower-left side of the table and identities on the upper-right. **b**, Transducerome screening of 5-HT$_{5A}$R using TRUPATH platform by the endogenous agonist 5-HT. Net BRET values of 5-HT$_{5A}$R together with positive controls of either neurotensin receptor 1 (NTSR1, agonist NT1-13) or β_2AR (agonist isoproterenol) are shown in each panel. Data represent mean ± SEM of N = 3 biological replicates.

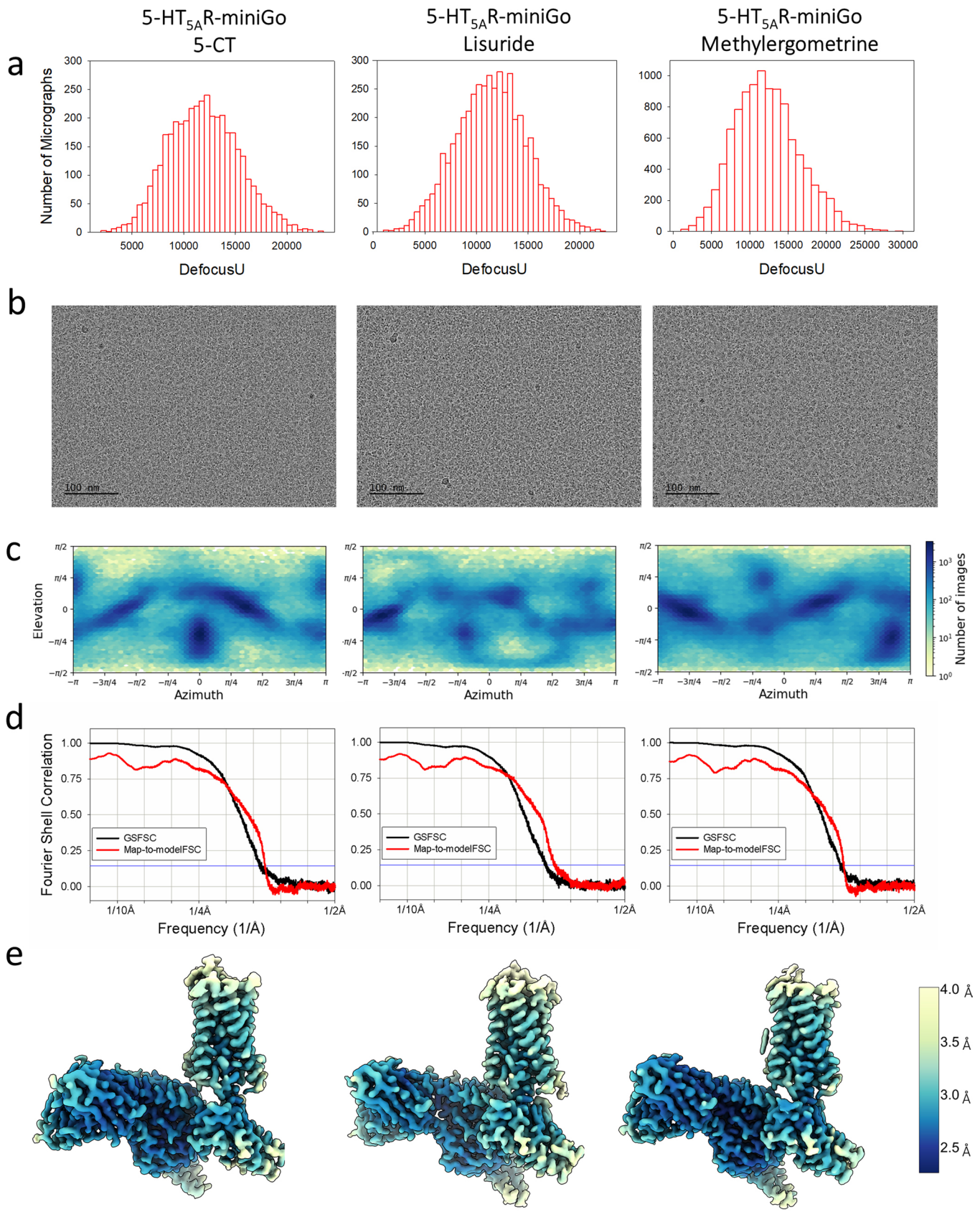

Extended Data Fig. 2 | See next page for caption.

Extended Data Fig. 2 | CryoEM analysis for 5-HT$_{5A}$R-miniGo bound to 5-CT, Lisuride, and Methylergometrine. For each of the respective agonist bound 5-HT5AR heterotrimeric complexes are shown: **a**, Histograms of defocus values for micrographs used in the single-particle analysis (see Table 2 for more details). **b**. Representative frame aligned micrograph. The experiment was repeated three times with similar results. **c**, Orientational distribution heat map. **d**, 2D plots of the gold-standard Fourier shell correlation (GSFSC) between half maps (black) and FSC between model and the B-factor sharpened map for respective refined model (red) as calculated by Phenix.mitrage. **e**, Local resolution heat-map calculated using the local windowed FSC method.

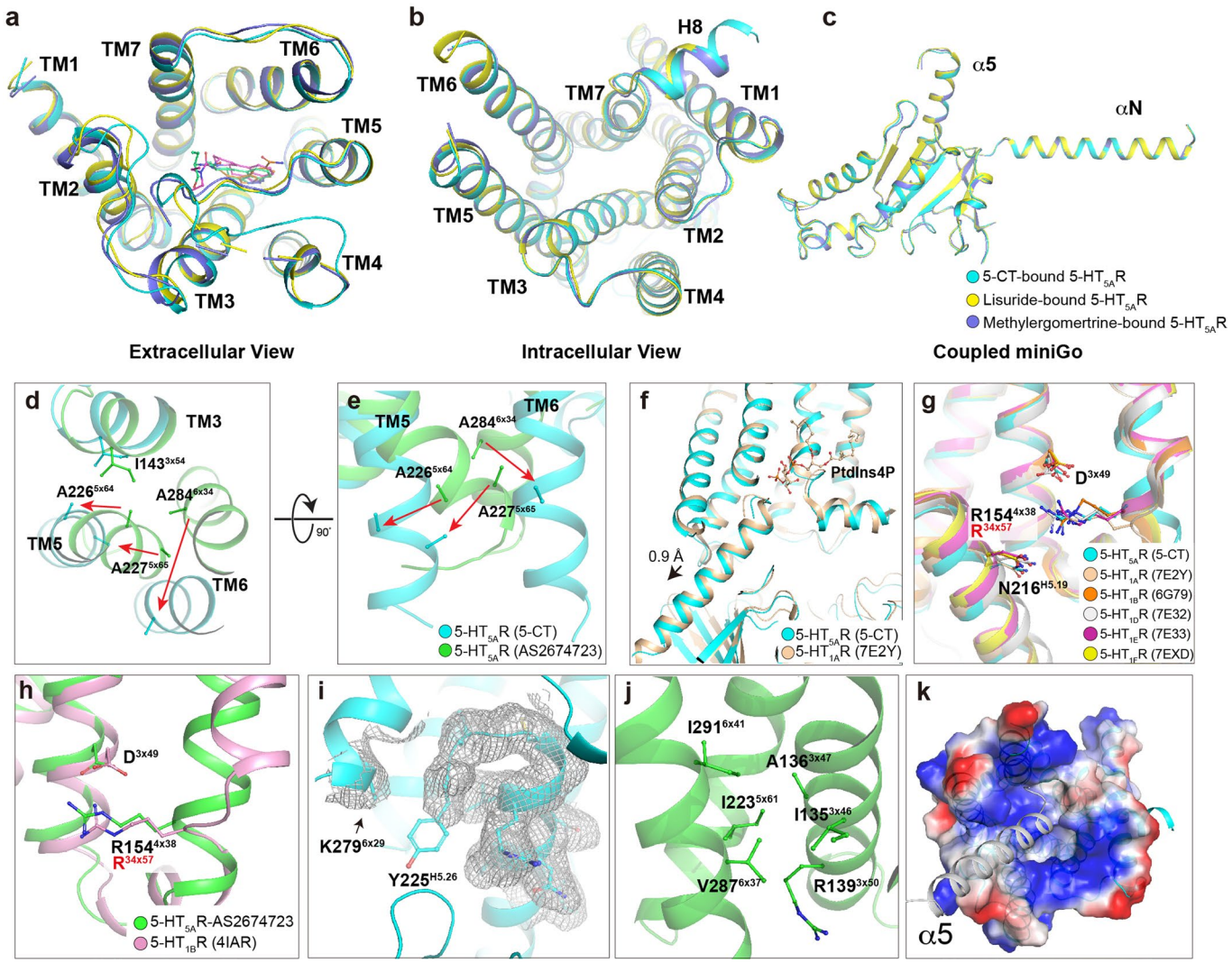

Extended Data Fig. 3 | Comparisons of 5-HT$_{5A}$R structures and the interface between 5-HT$_{5A}$R and miniGo protein. a-c, Extracellular and intracellular views of receptors (a-b) and G proteins (c) from the superpositions of the three agonist-bound 5-HT$_{5A}$R complexes. **d-e**, two views of the displacements of three alanines in the 3 A cluster upon the receptor activation. The movements of the residues are indicated by the red arrows. **f**. superposition of the 5-CT-bound 5-HT$_{5A}$R structure with the active state 5-HT$_{1A}$R structures. The PtdIns4P molecule is shown in sticks. **g-h**, Interactions between the R4x38 or R34x57 and D3x49 in the active (g) and inactive (h) 5-HT$_{5A}$R structures. **i**, Representative density maps of Y225$^{H5.26}$ and K279^{6x29}. **j**, Interactions between the V287^{6x37} and surrounding residues in the inactive 5-HT$_{5A}$R structure. **k**, The electrostatic potential surface of 5-HT$_{5A}$R from the intracellular side and interaction with the α5 helix of miniGo.

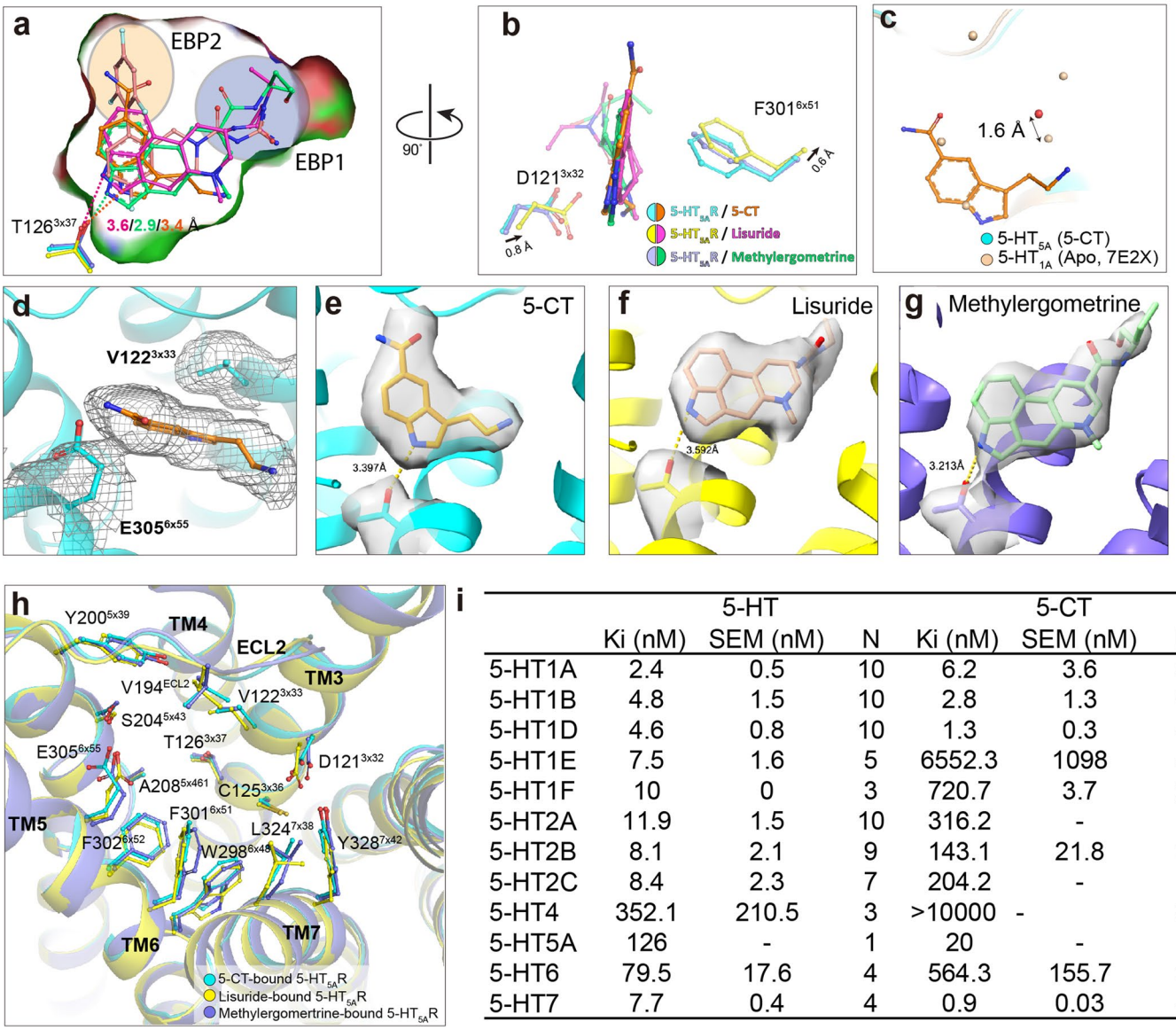

i

	5-HT			5-CT		
	Ki (nM)	SEM (nM)	N	Ki (nM)	SEM (nM)	N
5-HT1A	2.4	0.5	10	6.2	3.6	6
5-HT1B	4.8	1.5	10	2.8	1.3	9
5-HT1D	4.6	0.8	10	1.3	0.3	5
5-HT1E	7.5	1.6	5	6552.3	1098	4
5-HT1F	10	0	3	720.7	3.7	2
5-HT2A	11.9	1.5	10	316.2	-	1
5-HT2B	8.1	2.1	9	143.1	21.8	3
5-HT2C	8.4	2.3	7	204.2	-	1
5-HT4	352.1	210.5	3	>10000	-	3
5-HT5A	126	-	1	20	-	1
5-HT6	79.5	17.6	4	564.3	155.7	3
5-HT7	7.7	0.4	4	0.9	0.03	4

Extended Data Fig. 4 | Ligand binding pocket of 5-HT$_{5A}$R. a-b, Two views of the superposition of ligands AS2674723, 5-CT, lisuride, and methylergometrine in the 5-HT$_{5A}$R binding site. The hydrogen bonds between T126 and three agonists are shown as dashed lines in the same color as the corresponding ligand, respectively. The positions of EBP1 and EBP2 are also indicated by the purple- and salmon-shaded ovals, respectively. **c**, Displacement of waters in the binding pocket of the apo 5-HT$_{1A}$R-Gi complex structure (PDB: 7E2X) compared with the water molecule in the 5-CT bound structure. **d**, The representative density map of E305 in the 5-CT bound 5-HT$_{5A}$R structure. **e-g**, cryo-EM maps of T126 and three agonists. The distances are indicated by the dashed lines. **h**. Structural alignment of the ligand-binding pockets of three agonist-bound 5-HT$_{5A}$R complexes. **i**. Binding affinities of 5-HT and 5-CT to all the members of the human serotonin receptor family from the Ki database of PDSP (https://pdsp.unc.edu/databases/kidb.php). Data represent mean ± SEM of N = 1-10 replicates based on the source from the Ki database.

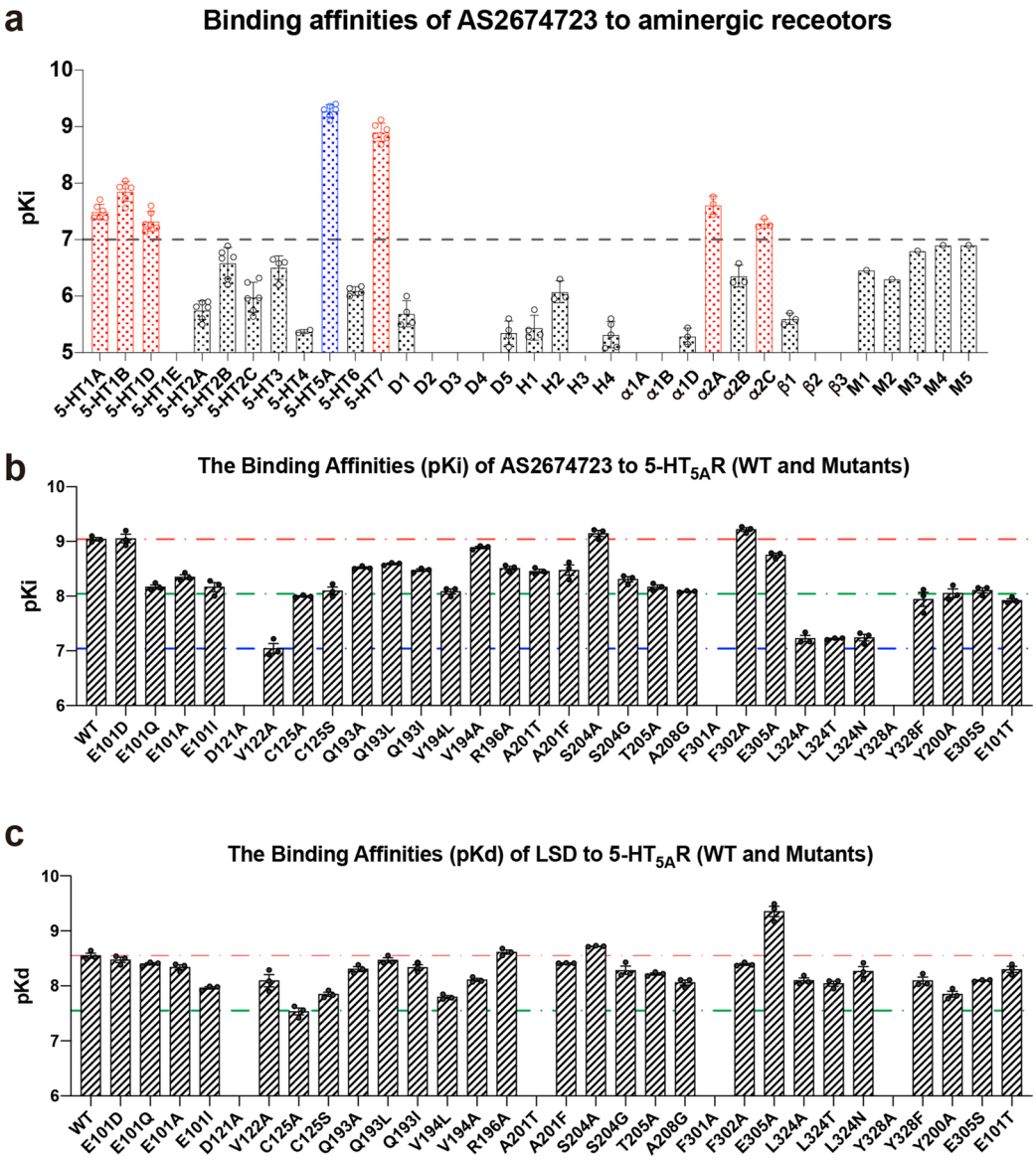

Extended Data Fig. 5 | Graphical representation of binding affinities. a, Binding affinities of AS2674723 against the aminergic receptors. Data represent mean ± SEM of N = 3-10 replicates (N = 1 for muscarinic receptors (M1-M5)). **b-c**, Binding affinities of AS2674723 and LSD for WT and mutant 5-HT_{5A}Rs using 3H-LSD. See Supplementary Table 11 for fitted parameter values that represent mean ± SEM of N = 3 biological replicates.

a

	Ligands Binding Pocket																			
	OBP								EBP1						EBP2					
GPCRdb	3x	3x	3x	3x	5x	6x	6x	6x	2x	3x	3x	45x	7x	7x	45x	5x	5x	5x	5x	6x
	32	33	36	37	461	48	51	52	64	28	29	51	38	42	52	39	40	43	44	55
Res.	121	122	125	126	208	298	301	302	101	117	118	193	324	328	194	200	201	204	205	305
5-HT5A	D	V	C	T	A	W	F	F	E	W	I	Q	L	Y	V	Y	A	S	T	E
5-HT1A	D	V	C	T	A	W	F	F	Q	F	I	T	N	Y	I	Y	T	S	T	A
5-HT1B	D	I	C	T	A	W	F	F	T	W	L	V	T	Y	V	Y	T	S	T	S
5-HT1D	D	I	C	T	A	W	F	F	T	W	L	L	T	Y	V	Y	T	S	T	S
5-HT1E	D	M	C	T	A	W	F	F	I	W	L	T	T	Y	I	Y	T	S	T	E
5-HT1F	D	I	C	T	A	W	F	F	I	W	L	I	A	Y	I	S	T	S	T	E
5-HT2A	D	V	S	T	S	W	F	F	I	W	I	L	V	Y	L	F	V	G	S	N
5-HT2B	D	V	S	T	A	W	F	F	I	W	L	V	V	Y	L	F	M	G	S	N
5-HT2C	D	V	S	T	A	W	F	F	I	W	I	V	V	Y	L	F	V	G	S	N
5-HT4	D	V	T	T	A	W	F	F	L	R	T	V	L	Y	F	Y	A	C	S	N
5-HT6	D	V	C	S	T	W	F	F	A	W	T	R	T	Y	L	F	V	A	S	N
5-HT7	D	V	C	T	A	W	F	F	D	F	I	L	L	Y	I	Y	T	S	T	S

b

	ICL2								3A Cluster			5-HT5AR-miniGo interface											
GPCRdb	34x	34x	34x	34x	34x	34x	34x	34x	5x	5x	6x	3x	3x	3x	34x	34x	4x	5x	5x	6x	6x	6x	8x
	50	51	52	53	54	55	56	57	64	65	34	50	53	54	51	57	38	61	68	32	36	37	47
Res.	146	147	148	149	150	151	152	153	226	227	284	139	142	143	147	153	154	223	230	282	286	287	342
5-HT5A	H	M	E	Y	T	L	R	T	A	A	A	R	S	I	M	T	R	I	R	R	M	V	N
5-HT1A	P	I	D	Y	V	N	K	R	A	A	V	R	A	I	I	R	T	I	R	K	T	L	N
5-HT1B	A	V	E	Y	S	A	K	R	E	A	T	R	A	I	V	R	T	I	R	K	T	L	N
5-HT1D	A	L	E	Y	S	K	R	R	A	A	T	R	A	I	L	R	T	I	R	K	I	L	N
5-HT1E	A	I	E	Y	A	R	K	R	A	A	A	R	A	I	I	R	T	I	L	K	I	L	N
5-HT1F	A	V	E	Y	A	R	K	R	A	A	A	R	A	I	V	R	T	I	L	K	T	L	N
5-HT2A	P	I	H	H	S	R	F	N	S	L	S	R	A	I	I	N	S	T	E	K	V	L	N
5-HT2B	P	I	Q	A	N	Q	Y	N	A	L	C	R	A	I	I	N	S	T	K	R	V	L	N
5-HT2C	P	I	E	H	S	R	F	N	V	L	S	R	A	I	I	N	S	T	Q	K	V	L	N
5-HT4	P	L	V	Y	R	N	K	M	T	A	A	R	A	I	L	M	T	I	H	K	T	L	N
5-HT6	P	L	R	Y	K	L	R	M	A	A	S	R	L	I	L	M	T	I	Q	K	T	L	M
5-HT7	P	L	T	Y	P	V	R	Q	A	A	A	R	G	I	L	Q	N	I	S	K	T	L	N

Extended Data Fig. 6 | Sequence alignments of 12 GPCR members of the 5-HT receptor family. a, Alignment of the residues in the ligand-binding pocket. **b**, Alignment of the residues in ICL2, 3 A cluster, and receptor-G protein interface.

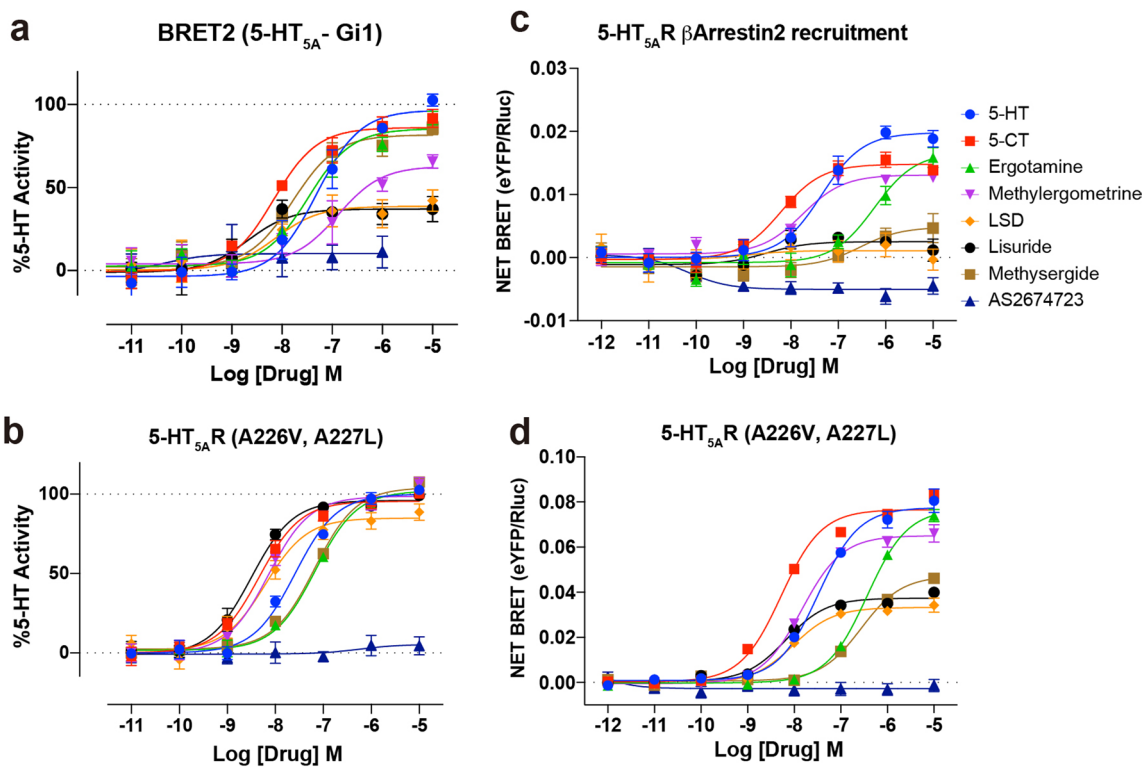

Extended Data Fig. 7 | Functional validation of the double mutant (A226V and A227L). a-b, BRET2 Gi1-activation assays and **c-d**, BRET1 β-arrestin2 recruitment of WT and double mutant (A226V and A227L) 5-HT_{5A}R stimulated by eight ligands. See Supplementary Table 12 for fitted parameter values that represent mean ± SEM of N = 3 biological replicates.

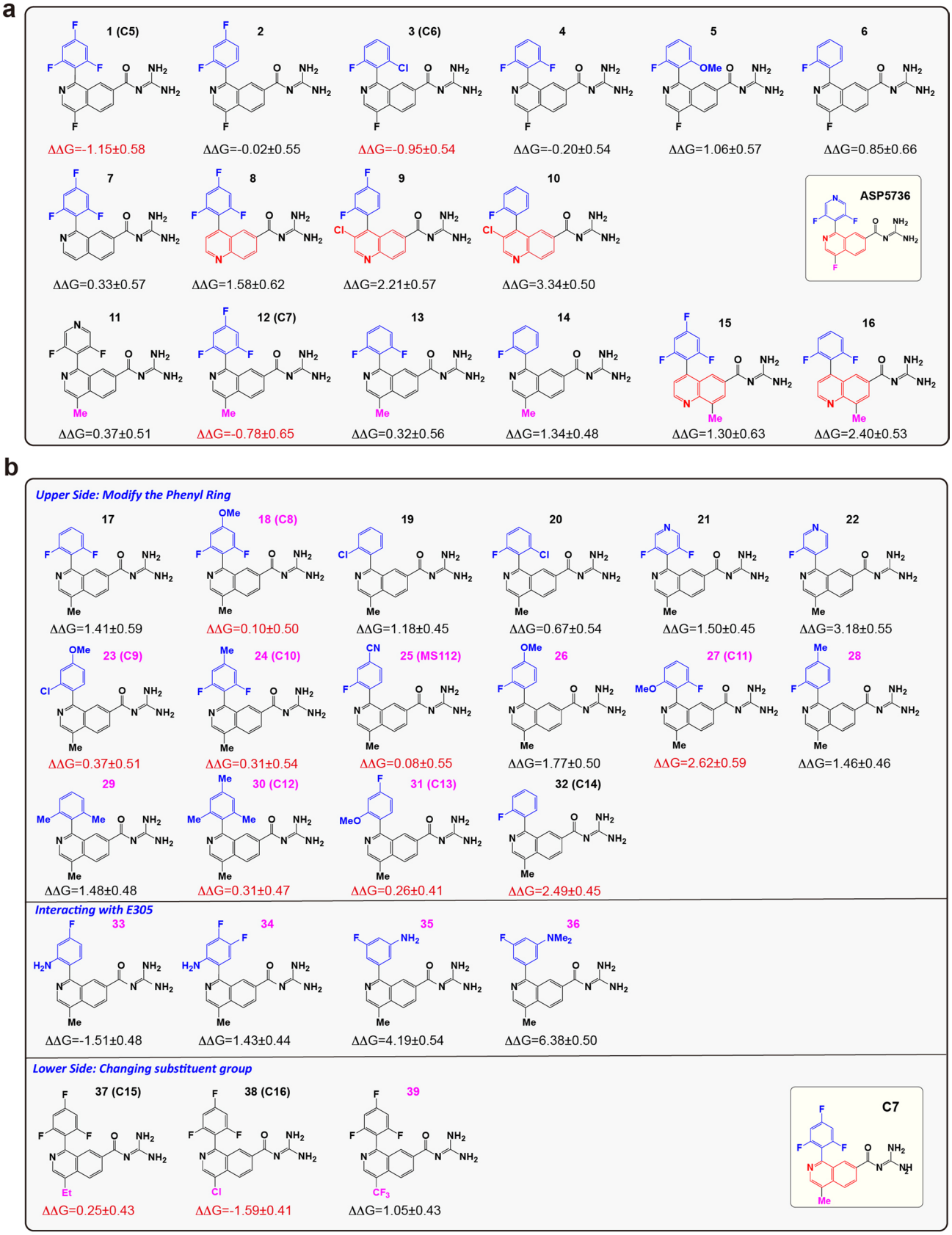

Extended Data Fig. 8 | Drug development of 5-HT$_{5A}$R. a-b, Chemical structures of all the designed compounds in the second (a) and third rounds (b) of structure-based drug development of 5-HT$_{5A}$R. Compounds with the ID colored in black or pink are selected from the patent or newly designed, respectively. The starting compound in each cycle is highlighted in a yellow shaded box. The varied moieties are colored in the corresponding color used in the starting compound. The predicted ΔΔG values by the FEP method are also labeled under the corresponding compound.

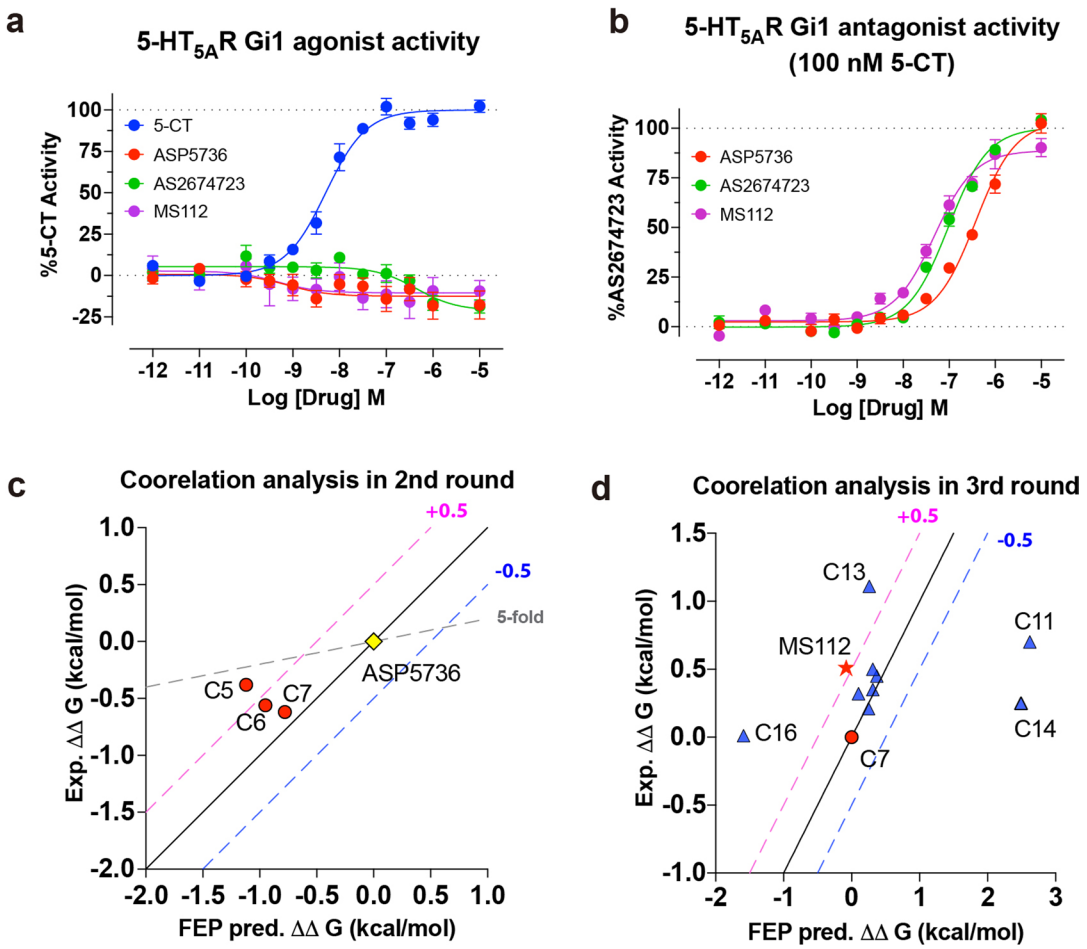

Extended Data Fig. 9 | Functional validation of the new selective compound MS112 and correlation analysis of FEP prediction. a-b, Agonist and antagonist activities tests of the compound MS112 towards 5-HT_{5A}R. See Supplementary Table 13 for fitted parameter values that represent mean ± SEM of N = 4 biological replicates. **c-d**, Correlation analysis between the predicted ΔΔG and experimental ΔΔG values. The dotted lines in both panels represent the ±0.5 kcal/mol between the FEP predicted ΔΔG and the experimental ΔΔG, respectively. And the +0.5 kcal/mol and −0.5 kcal/mol dotted lines are colored in magenta and blue, respectively. See Supplementary Table 14 for details.

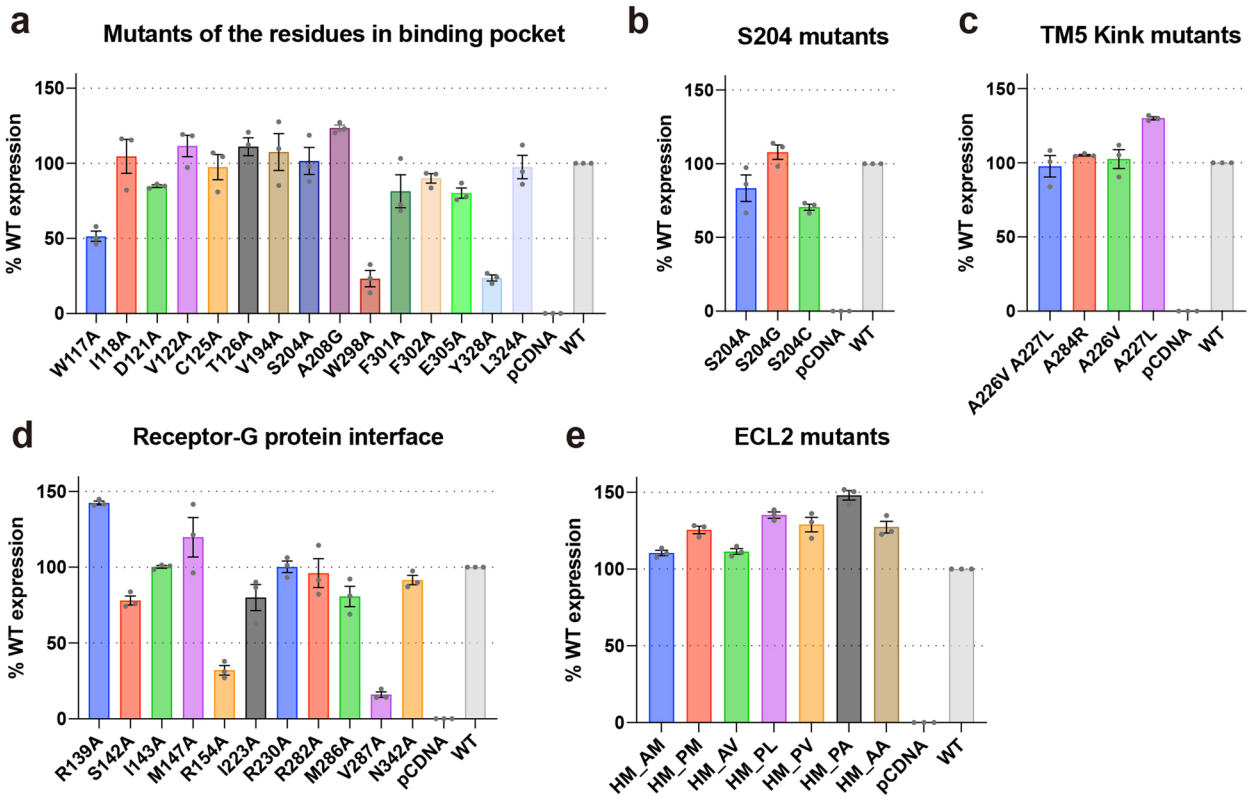

Extended Data Fig. 10 | Surface expression level of wt and mutant 5-HT$_{5A}$Rs. Data represent mean ± SEM of N = 3 biological replicates.

nature portfolio

Corresponding author(s): Jonathan F. Fay and Bryan L. Roth

Last updated by author(s): May 15, 2022

Reporting Summary

Nature Portfolio wishes to improve the reproducibility of the work that we publish. This form provides structure for consistency and transparency in reporting. For further information on Nature Portfolio policies, see our Editorial Policies and the Editorial Policy Checklist.

Statistics

For all statistical analyses, confirm that the following items are present in the figure legend, table legend, main text, or Methods section.

n/a	Confirmed
☐	☒ The exact sample size (*n*) for each experimental group/condition, given as a discrete number and unit of measurement
☐	☒ A statement on whether measurements were taken from distinct samples or whether the same sample was measured repeatedly
☒	☐ The statistical test(s) used AND whether they are one- or two-sided *Only common tests should be described solely by name; describe more complex techniques in the Methods section.*
☒	☐ A description of all covariates tested
☒	☐ A description of any assumptions or corrections, such as tests of normality and adjustment for multiple comparisons
☐	☒ A full description of the statistical parameters including central tendency (e.g. means) or other basic estimates (e.g. regression coefficient) AND variation (e.g. standard deviation) or associated estimates of uncertainty (e.g. confidence intervals)
☒	☐ For null hypothesis testing, the test statistic (e.g. *F*, *t*, *r*) with confidence intervals, effect sizes, degrees of freedom and *P* value noted *Give P values as exact values whenever suitable.*
☒	☐ For Bayesian analysis, information on the choice of priors and Markov chain Monte Carlo settings
☒	☐ For hierarchical and complex designs, identification of the appropriate level for tests and full reporting of outcomes
☒	☐ Estimates of effect sizes (e.g. Cohen's *d*, Pearson's *r*), indicating how they were calculated

Our web collection on statistics for biologists contains articles on many of the points above.

Software and code

Policy information about availability of computer code

Data collection	JbluIce-EPICS V2013.1 build 5287 (Crystallography), SerialEM V3.8.2 (CryoEM)
Data analysis	Structure determination and refinement: HKL3000, cryoSPARC V3.1.0, Topaz 0.2.2, DeepEMhancer, Relion3.1, UCSF Chimera 1.15, cisTEM 1.0.0-beta, PyMol 2.4.1, Coot 0.9.5, MolProbity (built in phenix 1.18.2), Phenix 1.18.2 Functional data analysis: GraphPad Prism 9.2 Ligand illustrator: ChemDraw 20.0. FEP analysis: Schrödinger modeling suite (v2020-4), PROPKa, Force Field Builder, FEP+

For manuscripts utilizing custom algorithms or software that are central to the research but not yet described in published literature, software must be made available to editors and reviewers. We strongly encourage code deposition in a community repository (e.g. GitHub). See the Nature Portfolio guidelines for submitting code & software for further information.

Data

Policy information about availability of data

All manuscripts must include a data availability statement. This statement should provide the following information, where applicable:

- Accession codes, unique identifiers, or web links for publicly available datasets
- A description of any restrictions on data availability
- For clinical datasets or third party data, please ensure that the statement adheres to our policy

The structures of the 5-HT5AR-AS2674723, 5-HT5AR-miniGo-5-CT, 5-HT5AR-miniGo-Lisuride, and 5-HT5AR-miniGo-Methylergomertrine have been deposited with the PDB (EMDB) under accession code 7UM4, 7UM5 (EMD-26597), 7UM6 (EMD-26598), and 7UM7 (EMD-26599). The cryoEM micrographs of 5-HT5AR-miniGo-5-

CT, 5-HT5AR-miniGo-Lisuride, and 5-HT5AR-miniGo-Methylergomertrine have been deposited in the EMPIAR database (https://www.ebi.ac.uk/empiar/) with accession numbers EMPIAR-11033, EMPIAR-11036, and EMPIAR-11039, respectively.

Field-specific reporting

Please select the one below that is the best fit for your research. If you are not sure, read the appropriate sections before making your selection.

☒ Life sciences ☐ Behavioural & social sciences ☐ Ecological, evolutionary & environmental sciences

For a reference copy of the document with all sections, see nature.com/documents/nr-reporting-summary-flat.pdf

Life sciences study design

All studies must disclose on these points even when the disclosure is negative.

Sample size	For cryoEM studies, the number of micrographs is determined by the available microscope time. For BRET and radioligand binding assays, number of technical replicates and biological replicates are reported in the figure legends. Sample size was determined based on variability of the response deviating from the mean as indicated by the standard error of the mean (SEM), which is also represented in the figures. Typically, at least three biological replicates were performed so that the SEM was within at least 20% of the mean, but exact number of replicates are indicated per result in figure legends.
Data exclusions	No data were excluded.
Replication	For BRET and radioligand binding assays, three biologically independent experiments (n=3) were performed. All attempts at replication were successful.
Randomization	For cryoEM study, meshes on the grids with good ice thickness were randomly allocated into experimental groups for data collection. For BRET and radioligand binding assays, randomization is not relevant as no group allocations were performed.
Blinding	No blinding was performed in this study. For both cryoEM structure determination and functional studies, blinding is not necessary due to the nature of these experiments do not requires subject assessment of the data that may influence the validity of the results

Reporting for specific materials, systems and methods

We require information from authors about some types of materials, experimental systems and methods used in many studies. Here, indicate whether each material, system or method listed is relevant to your study. If you are not sure if a list item applies to your research, read the appropriate section before selecting a response.

Materials & experimental systems

n/a	Involved in the study
☐	☒ Antibodies
☐	☒ Eukaryotic cell lines
☒	☐ Palaeontology and archaeology
☒	☐ Animals and other organisms
☒	☐ Human research participants
☒	☐ Clinical data
☒	☐ Dual use research of concern

Methods

n/a	Involved in the study
☒	☐ ChIP-seq
☒	☐ Flow cytometry
☒	☐ MRI-based neuroimaging

Antibodies

Antibodies used	gp64-PE antibody; anti-Flag–HRP-conjugated antibody
Validation	gp64-PE (R-PHYCOERYTHRIN (R-PE)-conjugated mouse anti-baculovirus monoclonal antibody is from mouse clone AcV1 and used for baculovirus titration. Detailed information can be found at: https://expressionsystems.com/product/gp64-pe-antibody/. anti-Flag–HRP-conjugated antibody is from mouse clone M2 and used for measuring protein expression on the surface of cells. Detailed information can be found at: https://www.sigmaaldrich.com/US/en/product/sigma/a8592.

Eukaryotic cell lines

Policy information about cell lines

Cell line source(s)	HEK293T cells were purchased from the American Type Culture Collection (ATCC, ATCC CRL-11268). Sf9 cells were obatined from Expression System (Cat 94-001S)

Authentication	HEK293T cells were authenticated by the supplier (ATCC) using morphology and growth characteristics, and STR profiling. Sf9 cells are commercial and obtained from vendors as indicated in the manuscript.
Mycoplasma contamination	HEK293T cells have been tested and shown to be free from mycoplasma (Hoechst DNA strain and Direct Culture methods employed). Sf9 cell line was certified as mycoplasma-free by the source company.
Commonly misidentified lines (See ICLAC register)	None